

Coincident In-situ and Triple-Frequency Radar Airborne Observations in the Arctic

Cuong M. Nguyen¹, Mengistu Wolde¹, Alessandro Battaglia^{2,3,4}, Leonid Nichman¹, Natalia Bliankinshtein¹, Samuel Haimov⁵, Kenny Bala¹ and Dirk Schuettemeyer⁶

¹Flight Research Laboratory, National Research Council Canada, Ottawa, K1A 0R6, Canada

²DIATI, Politecnico di Torino, Torino, Italy

³Earth Observation Science, Department of Physics and Astronomy, University of Leicester, Leicester, United Kingdom

⁴National Centre for Earth Observation, University of Leicester, Leicester, United Kingdom

⁵University of Wyoming, Laramie, USA

⁶European Space Agency, Noordwijk, NL

Correspondence to: Cuong M. Nguyen (Cuong.Nguyen@nrc-cnrc.gc.ca)

Abstract. The dataset collected during the Radar Snow Experiment (RadSnowExp) presents the first-ever triple-frequency radar reflectivities combined with almost perfectly co-located and coincident airborne in situ microphysics probes on board [a single platform](#), the National Research Council Canada (NRC) Convair-580 aircraft. ~~Over 12 hours~~[The potential of this dataset is illustrated here using data collected from one flight data in mixed-phased and glaciated clouds during an Arctic storm that covers a wide range of snow habits from pristine ice crystals, low density aggregates to heavily rimed particles with more than 3.4 hours in non-Rayleigh regions for at least one of the maximum size exceeding 10 mm. Three different flight segments with well-matched in situ and radar frequencies provide a unique opportunity for studying the relationship between cloud microphysical properties and radar measurements were analysed giving a total number of 49 minutes of triple-frequency signals observations.](#) The in situ particle imagery data for this study include imagery from the [Cloud Particle Imager \(CPI\)](#) probe, which provides high resolution [cloud particle imagery/images](#) and ~~allow~~[allows](#) accurate identification of particle types, including [level of riming/rimed crystals and large aggregates](#) within the [dual-frequency ratio \(DFR\)](#) plane. ~~The airborne triple-frequency radar data are analysed and~~ grouped based on the dominant particle compositions and microphysical processes (level of aggregation and riming). ~~The results from this study are consistent with the main findings of previous modelling studies, with specific regions of the dual-frequency ratio (DFR) plane associated with unique scattering properties of different ice habits, especially in clouds where radar signal is dominated by large aggregates. Moreover, the analysis shows that the close relationships between the triple-frequency signatures and particles-cloud microphysical properties (particle characteristic size, bulk density, and level of riming and aggregations and characteristic size of the particle size distribution (PSD)).~~

1 Introduction

There are currently two spaceborne atmospheric radars in operation: the [Global Precipitation Measurement Dual-frequency Precipitation Radar \(GPM-DPR\)](#) and the CloudSat [Cloud Profiling Radar \(CPR\)](#) whose missions have been foundational for characterizing the evolving nature of clouds and precipitation on Earth over the last decade. The [Cloud Profiling Radar \(CPR\)](#) on board CloudSat is a 94 GHz nadir-looking radar (Stephens et al., 2008), unique in its ability to sense condensed cloud particles whilst coincidentally detecting precipitation. While the CPR was not specifically designed for rain retrieval, its data have shown ~~a great potential also~~ for rain estimation ([Haynes et al., 2009](#)) and snowfall [estimation](#) in particular, providing vertical profiles of snowfall rate along with snow size distribution parameters and snow water content. ([Matrosov et al., 2008](#), [Hiley et al., 2011](#)). The joint NASA/JAXA GPM mission (Hou et al., 2014), launched at the end of February 2014, aims at providing global

measurements of precipitation with a higher accuracy and a wider coverage in latitudinal span (65°) than those obtained by the TRMM mission (Iguchi et al., 2000; Nesbitt and Anders, 2009). The GPM [Core Observatory](#) carries a Dual-Frequency Precipitation Radar (DPR) system including a Ka-band (35.5 GHz) radar and a Ku-band (13.6 GHz) radar. The GPM DPR detection performance ~~are~~ slightly improved compared to the TRMM precipitation radar (PR) with Minimum Detectable Signal (MDS) of 14.5 dBZ at Ku and 16.3 dBZ at Ka in the matched scan (MS) mode (Hamada and Takayabu, 2016). The inclusion of a second frequency in GPM has already demonstrated improvement in many aspects such as the ability to retrieve parameters characterizing the DSD in rain (Gorgucci and Baldini, 2016) and value in improving the rain classification (Le et al., 2016). Moreover, coincident measurements from the CloudSat CPR and the GPM DPR of the same precipitating system have illustrated that cm and mm-radars are effective in mapping different parts of the precipitating system and can be used synergistically in order to better retrieve cloud microphysical properties: [\(Battaglia et al., 2020a\)](#). Following the guidelines provided by the 2017 [NASA-2027 Decadal Survey](#); [\(National Academies of Sciences, Engineering, and Medicine, 2018\)](#), multi-frequency Doppler radars, with different combinations of Ku, Ka and W bands, have been proposed as the core instruments of the Aerosol Cloud Convection and Precipitation (A-CCP) mission GHz) (Kummerow et al, 2020, Battaglia et al., ~~2020b~~[2020a](#)). Multi-frequency radar observations are especially valuable in ice/snow cloud conditions because of the large variability in scatterers' microphysical properties (e.g. particle size, shape and density). The use of ~~multi~~[multiple](#) radar frequencies of which at least one is in or close to the Rayleigh regime (cm wavelength) and one is sufficiently affected by non-Rayleigh scattering (mm wavelength) has been proposed to improve retrievals of cloud properties over single-frequency applications (section 2). Better understanding of ice cloud characteristics and composition will relax assumptions made on the retrieval of precipitation rate of ice (von Lerber et al., 2017), and ice water content (IWC) which is needed to understand the global distribution of the ice-phase precipitation ~~and, therefore, thereby~~ enhancing our knowledge of the global water and energy budget.

Despite the valuable information the existing space-borne systems have been providing so far, gaps in the detection and characterization of precipitation remain, especially when the capabilities ~~in multi-frequency radar observations of ice/snow are considered (Battaglia et al., 2020b)~~[of multi-frequency radar observations of ice/snow are considered \(Battaglia et al., 2020a\)](#). [Triple frequency measurements have been made using ground based campaigns \(e.g. the 2019 TRIPle-frequency and Polarimetric radar Experiment TRIPEX \(Dias Neto et al., 2019\); the 2015 Biogenic Aerosols Effects on Clouds and Climate \(BAECC\) field campaign \(Kneifel et al., 2015\)\). The Parameterizing Ice Clouds using Airborne Observations and Triple-frequency Doppler Radar Data \(PICASSO\) campaign \(Westbrook et al., 2018\) has also been making ground based triple-frequency measurements along with coincident in-situ aircraft measurements of the microphysics. The co-location is very accurate as the radar dish is steered automatically using the real-time position feed from the aircraft.](#) To date, very few airborne experiments (e.g. the 2003 Wakasa Bay Advanced Microwave Scanning Radiometer Precipitation Validation Campaign (Lobl et al. 2007), and the 2015 Olympic Mountains Experiment (OLYMPEX) (Houze et al., 2017)) collected triple-frequency radar observations but only with limited [near](#)-coincident airborne in situ cloud microphysical data ~~(e.g. For example, the OLYMPEX provides 2.2 hours of in-cloud data with Ku-Ka-W radar data and coincident microphysics, (Chase et al., 2018; Tridon et al., 2019). To At the best time of our knowledge this writing, there are no publicly available such-coincident multi-frequency radar and in situ airborne datasets from high-latitude regions where precipitation is dominated by shallow, low intensity, snow or mixed-phased precipitation.~~

The RadSnowExp (Wolde et al., 2019) is a multi-platform and multi-sensor study organized by the European Space Agency (ESA) and conducted by the National Research Council of Canada (NRC) and Environment and Climate Change Canada (ECCC) to address the pressing need for provision of precipitation measurements, locally and globally. The research flights were conducted in mid-latitudes and near the Arctic circle (Iqaluit, NU, Canada, ~63N), during the fall of 2018, [covering a wide large](#)

geographical region and [wide range of](#) microphysical conditions, at a temperature range -50 to 5 °C and altitude extending to 7 km ([Fig. 4 Wolde et al., 2019](#)). The flights focused on sampling precipitation systems where large aggregates and rimed particles were present in order to optimize the triple-frequency analyses. Multi-frequency radar observations were carried out by the NRC Airborne W and X-band (NAWX) radars ([Wolde and Pazmany, 2005](#)) and the University of Wyoming's Ka-band Precipitation Radar (KPR) (Haimov et al., 2018). In addition to the radars, the NRC Convair-580 aircraft was equipped with extensive in-situ and remote sensing sensors installed in various locations of the aircraft, including on the underwing and wingtip pylons, various locations of the fuselage, and inside the aircraft cabin (Fig. 2). The dataset collected in flight during the RadSnowExp campaign

[uniquely contains unique](#) features:

- [collocated/co-located](#), high resolution triple-frequency [radars/radar data](#) with near coincident in situ measurements;
- [data from](#) state-of-the-art in situ sensors covering the whole scale of atmospherically relevant hydrometeor diameters, from aerosol size to precipitation size, along with high resolution imaging probes for single-particle identification;
- complementary measurements of [atmospheres/atmospheric](#) state parameters and cloud phase detection.

In this study, airborne measurements are used to evaluate findings from recent multi-frequency radar modelling studies [on the multi-frequency](#) that relate such radar signatures [of to](#) ice particles of varying habits, shapes, and sizes in different precipitation systems including intensive snow events in the mid and high-latitude regions.

This paper is structured as follows. Section 2 details on theoretical studies of triple frequency / multi-frequency. In section 3, airborne data processing and methodology for the airborne triple-frequency analysis are described. In section 4, the experimental evaluation of triple-frequency study using the RadSnowExp dataset is presented. Finally, conclusions and discussions are given in section 5.

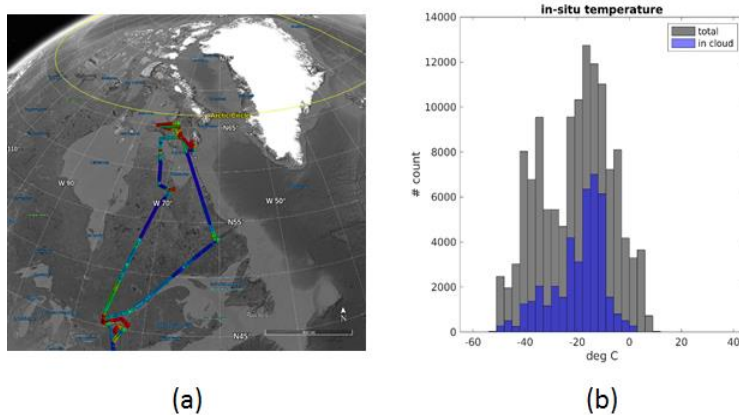


[Figure 1: Full flight path of the RadSnowExp campaign \(a\) and a histogram of the temperature range and frequency encountered in RadSnowExp flights \(b\).](#)

2 Multi-frequency radar ice retrieval potential

Multi-frequency radar observations are especially valuable in ice/snow cloud conditions. [Ice crystals complexity and](#) [The](#) large variability in [microphysical/ice crystal](#) properties ([e.g. such as](#) density, size, [and shape](#)) [make makes](#) the interpretation of single-frequency radar observations extremely challenging. The rationale for multi-frequency radar observations is detailed in recent papers (Ori et al., 2020; Battaglia et al., 2020a-b). In this section, we summarize some of the key results.

When comparing measurements of reflectivities from two radars operating at different frequencies f_1 and f_2 ($f_1 < f_2$), it is possible to consider the dual frequency ratios (DFR), defined as their difference in logarithmic units (equivalent to their ratio in linear units),

$$DFR_{f_1/f_2}(r)(dB) = Z_{f_1}^m(r) - Z_{f_2}^m(r) = \overbrace{Z_{f_1}^{nr}(r) - Z_{f_2}^{nr}(r)}^{\text{non-Rayleigh effect}} + \overbrace{2 \int_0^r (k_{f_2}^-(r) - k_{f_1}^-(r)) dr}^{\text{attenuation effect}} + \overbrace{2 \int_0^r (k_{f_2}^+(r) - k_{f_1}^+(r)) dr}^{\text{attenuation effect}} \quad (1)$$

where $Z_{f_1}^m(r)$ and $Z_{f_2}^m(r)$ are measured radar reflectivity factors in dBZ at range r and frequencies f_1 and f_2 , respectively; $Z_{f_1}^{nr}(r)$ and $Z_{f_2}^{nr}(r)$ are reflectivity factors due to non-Rayleigh effects. $k_{f_1}^-(r)$ and $k_{f_1}^+(r)$ denote specific attenuation (dB/km) at range r .

In equation (1), we have highlighted the two possible contributions to the DFR:

- “non-Rayleigh effects”, i.e. differences in the effective reflectivity factors of the targets which occur when the hydrometeor sizes are comparable to the radar wavelength (Bohren & Huffman, 1983; Lhermitte, 1990);
- “attenuation effects”, i.e. differences in the attenuation properties along the propagation path, with higher attenuations produced at higher frequencies (Lhermitte, 1990, Tridon et al., 2020).

Non-Rayleigh effects result from intensive properties of the PSD (e.g. characteristic size, spread of PSD) whereas attenuation effects can be used to infer extensive quantities (e.g. concentrations, rain rates, equivalent water contents). Because of the variety of ice habits and shapes, the computation of scattering properties of ice crystals is much more complex than for raindrops (Kneifel et al., 2020) and references therein; whilst at small sizes backscattering cross sections are proportional to the square of the mass of the crystals (Hogan et al., 2006), when approaching large sizes the mass distribution within the particle along the direction of the impinging radiation plays a key role in affecting the particle scattering properties (e.g. Hogan & Westbrook, 2014). An example of DFR calculations for exponentially and Gamma-distributed ice crystals is shown in Fig. 21 where data points diverge from the origin, which corresponds to the Rayleigh approximation when moving to larger sizes the particle size increases. There is clearly a large variability in the triple frequency observables introduced by the different shapes and degree of riming of the ice crystals as thoroughly demonstrated in Mason et al., 2019.

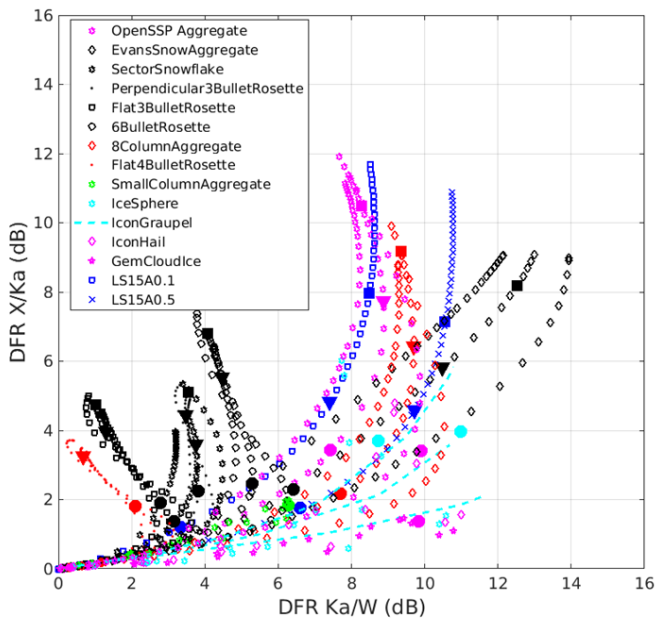
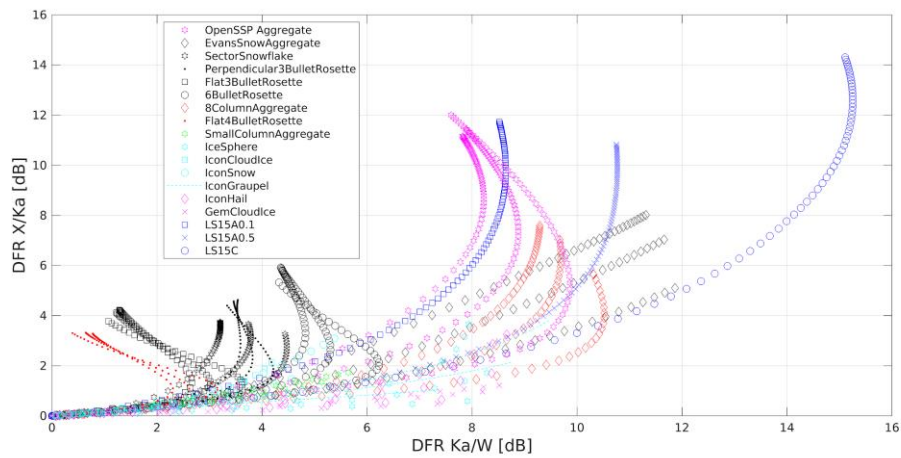


Figure 21: Example of DFR Ka/W vs DFR X/Ka corresponding to different populations of snow habits with different characteristic diameters of PSD. The habits correspond to state of the art scattering models: the first habit is a mixture of aggregates from the database described in Kuo et al., 2016; – the next 14 habits are extracted from the ARTS scattering database (Eriksson et al., 2018); the last three habits are from the models of Leinonen and Szyrmer, 2015. For the first two classes of models, scattering properties are computed via discrete dipole approximation for Gamma-PSD with equal the shape parameter μ equal -2, 0 and 8 (same symbols); for the last class the self-similar Rayleigh Gans approximation (for the corresponding coefficients see details in Mroz et al., 2021a) is used with exponential PSDs. The characteristic mean mass-weighted maximum size of the particles size distribution increases with the curve

moving out from the origin (that corresponds to Rayleigh particles with all DFRs being equal to zero). For each line the thick filled circle, triangle and square markers represents values of D_m equal to 2, 4 and 6 mm respectively.

140 **3 Data and methodology**

3.1 Airborne radars

In this study, triple frequency radar data from the NRC airborne W- and X-band radar (NAWX) and the Wyoming K-band Precipitation Radar (KPR) measurements from nadir and zenith looking antennas are used. The NAWX antennas are housed inside an unpressurized blister radome mounted on the right side of the aircraft fuselage (Fig. 3a2a) and the KPR radar was installed on the left wingtip pylon. Some important radar parameters are given in Table 1. More detailed information on the NAWX radar system and KPR can be found in Wolde and Pazmany (2005) and Haimov et al. (2018), respectively. In the RadSnowExp project, the radar complex I and Q samples are processed to powers and complex pulse pair products according to the radar parameter specifications table. ~~These products are recorded in binary format.~~ Although the three radars are almost ~~collocated~~co-located, additional signal processing steps are needed to provide the highest level of radar volume matching to reduce the DFR estimation errors and to provide the best evaluation of the radar measurements in synergy with in situ microphysics observations.

Table 1: Radar parameters for the RadSnowExp campaign.

Parameter	W-band	Ka-band	X-band
RF output frequency	94.05 GHz	35.64 GHz	9.41 GHz \pm 30 MHz
Nadir/Zenith antenna beamwidth	0.75°	4.2°	4.5°
Pulse width	500 ns	250 ns/2.5 μ s or 500 ns/5 μ s (short pulse/chirp)	500 ns
Range resolution	75 m	30 m 60 m	75 m
Dwell time	0.14 s	0.2 s	0.23 s
Sampling resolution	17.13 m or 34.26 m	15 m or 30 m	30 m

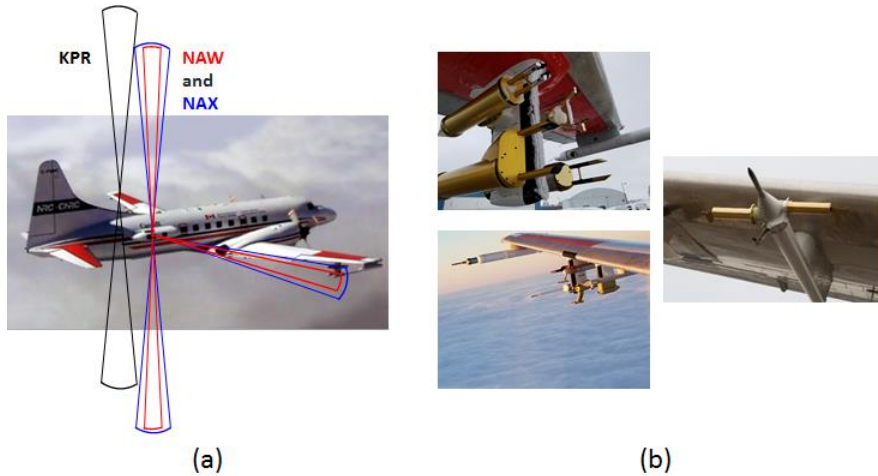


Figure 3-2: (a) Locations and direction of NAWX and KPR radars and antennas beams (a) and (b) wing-mounted microphysics sensors and air data probes (b).

3.1.1 Radar data volume matching

To obtain accurate estimates of DFR, radar reflectivity observations at each frequency would optimally sample the exact same volume; that is, the observations would have perfectly matched horizontal and vertical resolutions, and would be obtained simultaneously. This is not the case with the RadSnowExp dataset due to mismatched radar beamwidths, vertical resolutions and radar data dwell times. Hence, additional processing steps are needed to mitigate these mismatches. The 3 dB beamwidths and vertical sampling of the Ka- and X- band radar are $4.2^\circ / 30$ m and $4.5^\circ / 30$ m, respectively, whereas those of the W-band are $0.75^\circ / 34.26$ m. The volume matching procedure is described in the following steps.

- Re-alignment of data along the range axis: during aircraft rolls, distance from KPR (mounted on the aircraft wingtip) to the radar volume can be slightly different from that of NAWX. Re-aligning radar data along the range axis is ~~needed~~required. The re-alignment of the KPR data with the NAWX radar was done by using the ground as a reference point. We observe in most cases ~~that~~ range alignment for KPR is within 30 m.

- Smoothing: this step is ~~done~~performed to reduce the effect of the beamwidth and vertical sampling mismatch. At close range (~~500~~~245 m) where radar resolution volumes are small, we assume that the condition of uniform beam filling is met. First, a boxcar average filter with window length of 6 radar samples is applied to NAW data along the time axis. Resultant NAW data will have an effective beamwidth of 4.5° along the flight path which is close to that of NAX and KPR radars. Secondly, ~~data from the three radar data~~radars are mapped ~~into~~onto a common range axis with ~~the origin at the aircraft location and a resolution grid~~ of 35 m which is close to the vertical sampling of NAW. Next, measurements from the three radars are temporally averaged to 0.5 seconds. Vertical profiles were recorded every 0.14, 0.23, and 0.2 seconds for NAW, NAX and KPR, respectively, and then averaged in post-processing to one profile every 0.5 seconds. ~~This simple smoothing algorithm would mitigate the volume mismatch due to the radar location differences (the NAW and NAX radars are collocated but the KPR is about 10 m away) given an assumption of reasonable homogeneity of the scatterers within a few hundred meters around the aircraft. Finally, collocated~~Consequently, ~~co-located~~ triple frequency radar data are binned into a common grid of 0.5 seconds x 35 m (time - range) or 50 m x 35 m at the Convair average ground speed of 100 m s^{-1} . ~~This simple smoothing algorithm~~

mitigates the volume mismatch due to the radar location differences (the NAW and NAX radars are co-located but the KPR is about 10 m away), given the assumption of cloud homogeneity within 50 m along the flight path.

3.1.2 Radar close range DFR calibration fine tuning at close range

Calibration for NAWX nadir antennas is made using clear air observations of the water surface backscatter cross section (Li et al., 2005). Calibration for other NAWX antennas and KPR is done by comparing measurements between antenna ports. More details on calibration and results for NAWX and KPR radars are described in WoldeNguyen et al. (2019) and Nguyen and Wolde (2021). Figure 43 shows an example of radar vertical reflectivity profiles from nadir antennas for a RadSnowExp flight on 22 November 2018. At those sampling times, data from in situ imaging probes (not shown) indicate that the aircraft sampled a region of small ice particles with median volume diameters (MVD) less than 300 μm which is in the Rayleigh scattering region of the three radars (see Table A1 in Battaglia et al., 2020a), i.e. all equivalent the difference between reflectivity factors at Ka band and W band is negligible and between X band and Ka band is about 0.2 dB (Matrosov, 1993). Hence, the differences in the equivalent reflectivities from the three frequencies should be the same mainly depend on the frequency differences of the dielectric factors ($|K_w|^2$). However, it can be seen that, at distances within 700 m from close to the aircraft radars there is disagreement large mismatches between the measurements and the mismatches become larger at closer ranges (Fig. 3b). This is explained by the limitations of the radar hardware that affects the measurements at this range, within a few first pulse lengths: when the receivers reach to their steady state. For this study, it is critical to obtain reliable radar data that are as close as possible to the aircraft so that the radar and the in situ sensors sample nearly the same volume. In addition, at near close distances, the effect of radar attenuation on the radar reflectivity is minimal. Within a couple of hundred meters, radar attenuation at Ka and X band in snows/ice clouds is negligible. W-band attenuation caused by atmospheric gases, water vapour and ice scattering in snows/ice clouds would be also minimal at a distance < 300 m. Data at the first few range gates in the far field distance of the radars, collected in regions of small ice particles near cloud tops, were used to compare the W band to the X and Ka band. Results show that, at a range of 245 m, the W-band is used as a reference because of its better sensitivity level and the first usable range gate (where the data is usable (not affected by close range biases; 2)) is smallest, at 245 m. Results show that, at a range of 245 m, the relative offsets between W-X and W-Ka are nearly constant for each flight. When those offsets are removed, dual When the offset correction is made and the frequency ratio (DFR) estimates dependent dielectric properties of the scatterer are taken into account (i.e. a common $|K_w|^2$ is used for all three frequencies), the DFR Ka/W should be unbiased. The DFR uncertainty 0 dB and the DFR X/Ka ~ 0.2 dB. This choice is also consistent with the forward modelling approach in calibration section 2. Figure 4 shows the joint distribution of adjusted reflectivities for the two frequency pairs at regions of small ice particles (MVD < 300 μm) for the whole 22 November flight. In general, the biases in the DFR estimates are less than 1 dB and the standard deviations is estimated to be less than 0.577 dB and 0.8 dB for DFR Ka/W and DFR X/Ka, respectively. It is noted that below -5 dBZ, KPR signal becomes noisy due to the system's low sensitivity so are excluded in the analysis.

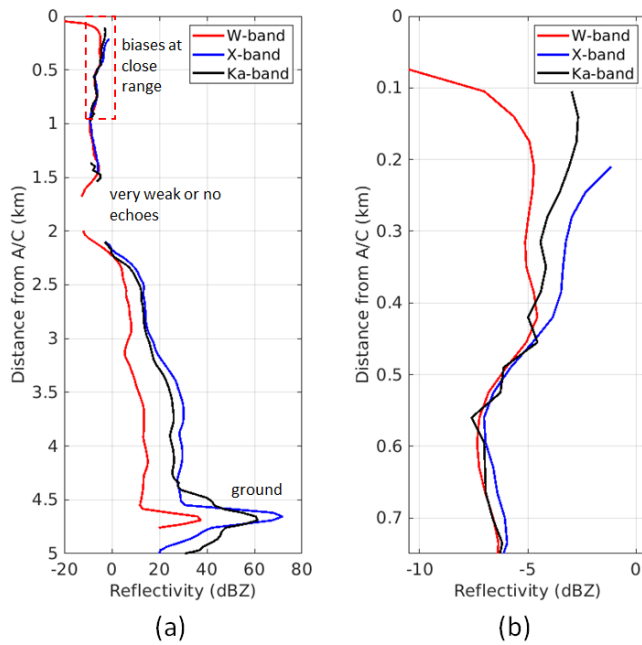


Figure 10d shows reflectivity observations at 245 m away from the aircraft after correcting for close range biases for the entire flights on 22 November 2018. It was verified that 1) relative radar calibration is good across the whole flight (excellent agreements of triple frequency reflectivity in regions of small particles); 2) radar volume matching and time synchronization are good (fine scale features were consistently captured by three radars). It is noted that at 245 m distance below -5 dBZ, KPR signal becomes noisy, due to the system's low sensitivity so are excluded in the analysis.

215

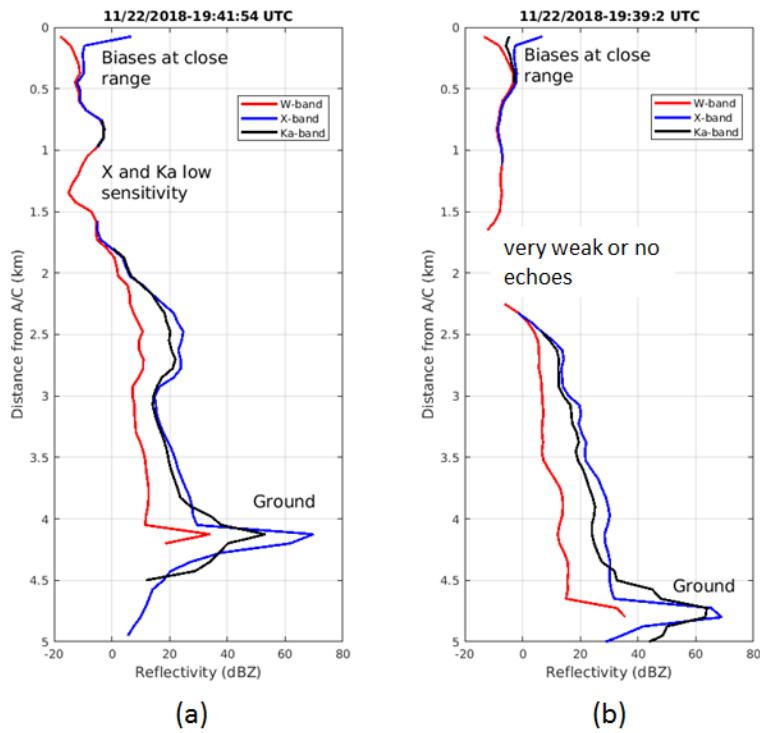


Figure 4: Examples3: (a) Example of vertical profiles from three radars showing different scattering regimes and (b) close-up plot showing the mismatch of triple-frequency measurements at in close ranges. range region indicated by a box in (a).

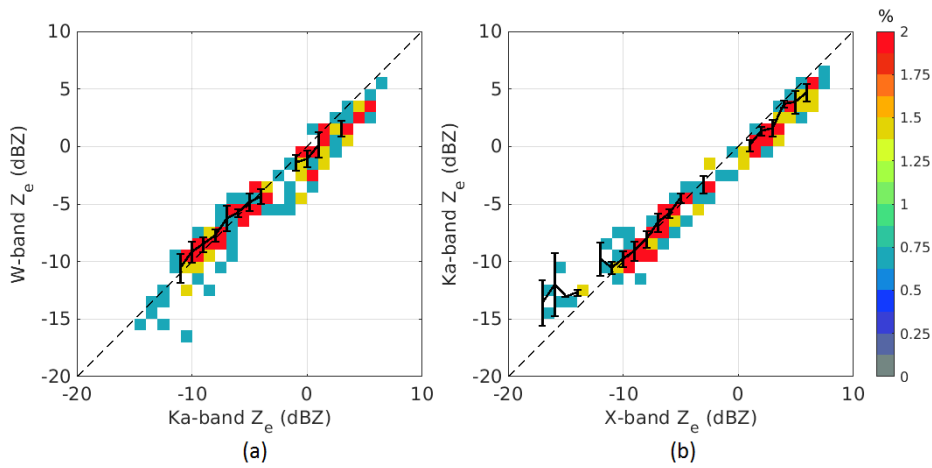


Figure 4: Scatterplots of (a) W-band and Ka-band, and (b) Ka-band and X-band cross-calibrated reflectivities at 245 m from the nadir antennas for the Nov 22 flight. The data are thresholded by $MVD < 300 \mu m$ and are binned on a 2D grid with grid size of 0.5 dB. The dashed black line is the 1:1 line. The solid black lines are the mean curve and one standard deviation error bars.

3.2 In situ sensors

For the RadSnowExp project, the NRC Convair-580 aircraft owned and operated by the NRC, was jointly instrumented by NRC and Environment and Climate Change Canada (ECCC) with state-of-the-art in-situ sensors for measurements of aircraft and atmospheric state parameters, and cloud microphysical properties. Bulk liquid water content (LWC) and total water content (TWC) were measured simultaneously with particle images and size distribution, ranging from small cloud droplets ($< 10 \mu\text{m}$) to large precipitation hydrometeors ($> 10 \text{mm}$).

For this work, the cloud particle size distribution was composed using a combination of data from several single-particle probes: Fast Cloud Droplet Probe (FCDP, 2-50 μm , SPEC Inc.); two-dimensional stereo (2DS, 10-1200 μm , SPEC Inc.) probe; High Volume Precipitation Spectrometer version 3 (HVPS3, 150-19200 μm , SPEC Inc.) probe and Precipitation Imaging Probe (PIP, 100-6400 μm , DMT). The probes are equipped with anti-shattering tips (Korolev et al., 2013a) and were calibrated with glass beads and a spinning chopper before the campaign and re-evaluated in NRC's altitude icing wind tunnel after the campaign. The uncertainties in sizing and concentrations were less than 5%. Taking into account image corrections and rejections, the propagated uncertainties can grow within the range presented by Baumgardner et al. (2017). The single-particle data are then used to derive size distributions and bulk cloud properties.

probe or Precipitation Imaging Probe (PIP, 100-6400 μm , DMT). In addition, Cloud Particle Imager (CPI, 10-2000 μm , SPEC Inc.) provided high resolution (2.3 μm) grayscale imagery of small cloud and drizzle drops, ice particles and portions of large drops and ice crystals and broken large ice particles. The high resolution of the CPI probe allows identification of riming levels on ice crystals. In order to aid the determination of triple frequency radar signatures of various particle compositions and level of riming, the CPI images were classified into 24 different hydrometeor types using machine learning with Convolutional Neural Network method (similar to Praz et al., 2018) based on a training dataset created from recent projects conducted using the NRC Convair-580. For this paper, we combined some of the classifications and reduced the grouping to nine different types (Table 2). CPI data integrated over 5 seconds are used to compute and to plot the fractions of sampled particle types. For each study case, we present two CPI particle fraction plots, one for all 9 groups listed in Table 2 and one for a subset of ice habits only. The fraction plots are presented in section 4.

Table 2: CPI classification grouping definitions

Merged group	Ice particle types
Pristine	Columns, capped columns, bullets, bullet rosettes, plates,
Dendrites	Stellar dendrites, blurred dendrites
Rimmed dendrites	Rimmed dendrites
Rimmed particles	Graupels, densely rimmed, rimmed columns
Aggregates	Aggregate columns, aggregate planars
Other ice particles	Two-drops, blurred ice, broken triangle, ice, melting large, semi-spheroid, tiny ice
Small particles	Particles $< 40 \mu\text{m}$
Drops	Drops, blurred drops
Artifact	Artifact

Particle size detection range of each probe is illustrated in Fig. 5. The probes were calibrated with glass beads and a spinning chopper before the campaign and re-evaluated in NRC's altitude icing wind tunnel after the campaign. The uncertainties in sizing and concentrations were less than 5%. Taking into account image corrections and rejections, the propagated uncertainties

can grow within the range presented by Baumgardner et al. (2017). The single particle data are then used to derive size distributions and bulk cloud properties.

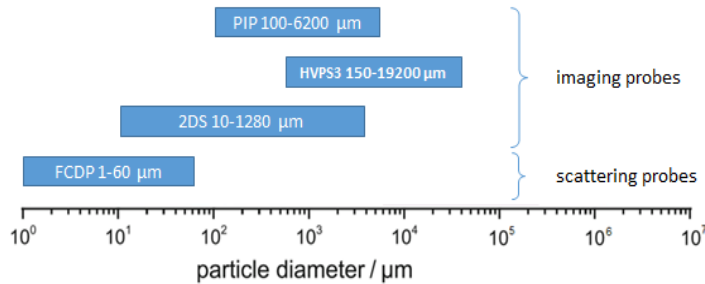


Figure 5: Single particle detection ranges of FCDP, 2DS, HVPS3 and PIP, jointly covering the broadest detectable range of single particle diameters.

TWC and LWC were measured by the Nevzorov, a constant-temperature, hot-wire probe (Korolev et al., 1998). The sensitivity of Nevzorov is estimated to be up to $0.002-0.002 \text{ g m}^{-3} \text{ m}^{-3}$ (Abel et al., 2014). We estimate the accuracy of the Nevzorov measurements during RadSnowExp to be on the order of 0.05 g m^{-3} , similar to the estimation provided by Faber et al. (2018). Additionally, the Nevzorov ice water content measurements can be subject to increased uncertainty when large hydrometeors are present. It should be noted that the probe is analog and thus prone to artifact originating from aircraft wiring. However, this noise was simultaneous in collector and reference wires and thus had little effect on the estimated water content. We estimate the accuracy of the Nevzorov data during RadSnowExp to be on the order of 0.05 g m^{-3} . (Schwarzenboeck et al., 2009 and Korolev et al., 2013b).

Additionally, the composite PSD, derived from single particle probes, is used to calculate characteristic sizes (Median Volume Diameter - MVD), and concentrations (N). We set a 50 μm lower bound for $N(D)$ in calculating total volume within PSD, and MVD. This will minimize the impact of supercooled drops in the calculations and interpretation of parameters characterizing ice particles. The exclusion of small particles does not have a major impact on the calculated bulk microphysics (i.e. bulk density and MVD) and radar reflectivity, which are dominated by large particles. Several The definitions of several bulk microphysical parameters calculated from the measured PSDs are given below.

- Effective bulk density (ρ_e) is the ratio of the mass of ice to the total volume of ice within a sample volume. An empirical method to compute ρ_e from PSD (Heymsfield et al., 2004; Chase et al., 2018) is defined as,

$$\rho_e = \frac{m_{TWC}}{V} \frac{IWC}{V} \quad (2)$$

where m_{TWC} is the mass of ice inferred from power dissipated on TWC and LWC sensors of the Nevzorov probe (Korolev et al., 1998), with units of g m^{-3} and V is calculated as the sum of the volume of all particles within the PSD, with units of $\text{cm}^3 \text{ m}^{-3}$. Thus ρ_e has units of g cm^{-3} . Here, each particle is approximated as an oblate spheroid with an aspect ratio of 0.6 (Hogan et al., 2012). Both m_{TWC} and V are computed for 1 m^3 .

- Median volume diameter (MVD) is defined as the diameter for which the total volume of all drops having greater diameters is just equal to the total volume of all drops having smaller diameters. This is the in situ derived MVD will be used to evaluate the relationship between the characteristic diameter that contributes most to cloud liquid water or mass. Calculation size of MVD is the PSD and the DFRs (Kneifel et al., 2015). MVD can be described in Leroy et al. (2016) as,

$$\int_{D_{min}}^{MVD} V(D)N(D)dD = \int_{MVD}^{D_{max}} V(D)N(D)dD \quad (3)$$

Formatted: Bullets, No bullets or numbering, Border: Top: (No border), Bottom: (No border), Left: (No border), Right: (No border), Between: (No border)

Formatted: Font color: Auto

where $V(D)$ is the volume of a particle as a function of size and is calculated in the same way as in the calculation of effective bulk density.

- Particle number concentration (N_t):

$$N_t = \int_{D_{min}}^{D_{max}} N(D) dD \quad (34)$$

In order to show how often we encountered regions that are interesting targets for triple frequency radars, the complementary cumulative distribution functions of MVD from PSD are calculated for three of the Among the three RadSnowExp project flights (22, 25 and 28 November 2018; Fig. 6). Among the three flights, two of flights were carried out in the Arctic (22 and 25 November) and the one of the flight third was conducted in mid-latitude. It can be seen that in one of The case studies we are looking at are from the flights (the 22 November, 2018), 13% of the sampling points, which we chose because larger values of MVD were in the non-Rayleigh region for all three frequencies whilst there were almost surely no similar sampling point for more frequent than during the other arctic flight (25 November in Fig. 6). For this reason, the analysis in this paper is focused on the arctic flight conducted on 22 November 2018. two flights.

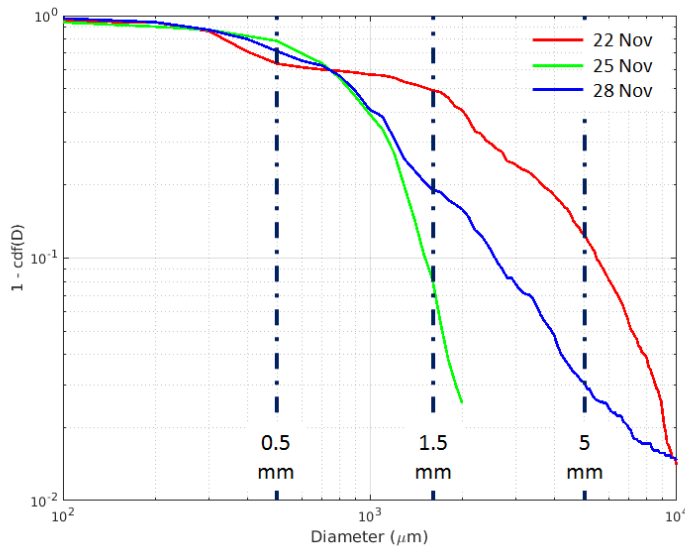


Figure 6: The complementary cumulative distribution functions of particle diameter from PSD for flights on 22, 25, and 28 November 2018. As a rule of thumb non-Rayleigh effects of the order of 1 dB appear for diameters exceeding 0.5, 1.5 and 5 mm at W, Ka and X, respectively (see Table A1 in Battaglia et al., 2020b).

3.3.3 Collocating Co-locating radar and in situ measurements

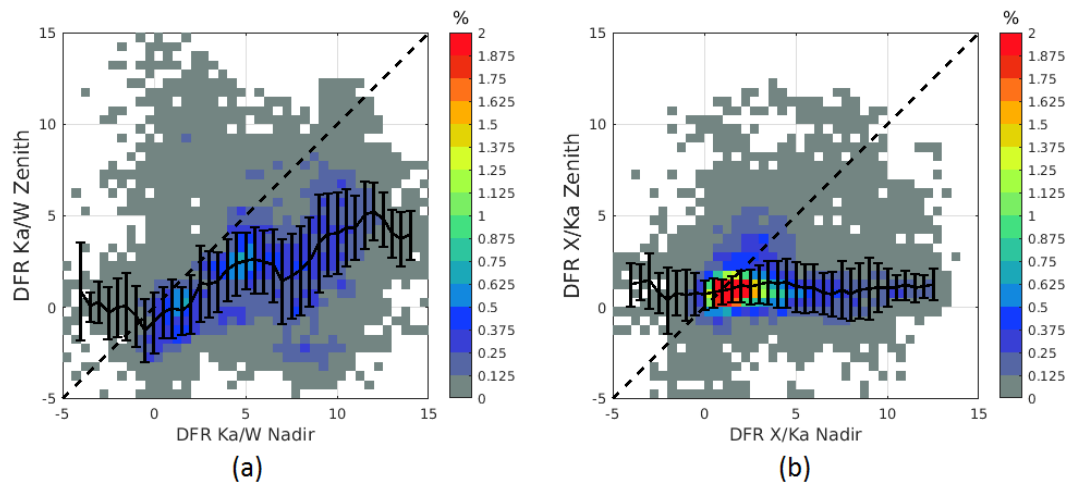
Collocating Co-locating radar and in situ measurements is a critical step for accurate determination of relations between microphysics and radar scattering properties. Coincident measurements and perfectly matched volumes would provide the most accurate assessment. However, in reality, radar sampling volumes are much larger than those of cloud probes and both sample volumes are not spatially collocated. In literatures, collocating co-located. In the literature, co-locating radar and in situ data is often archived by averaging radar data over a large time such as in ground based observations (Kneifel et al., 2015); or alternatively finding the nearest airborne radar data points to the in situ measurements (Chase et al., 2018;). For example, in

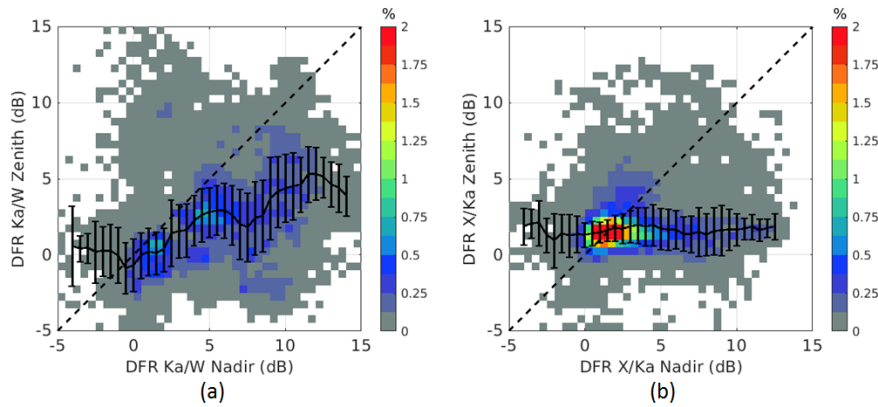
Chase et al. (2018), radar and in situ data were obtained from two different platforms and post-processing algorithms assumed that radar volumes within 10 min temporally and 1 km spatially of in situ were considered ~~collocated~~co-located. Moreover, the in situ observations were assumed to be characteristic of the entire matched radar volume despite the differences in the radar and probes sample volumes.

In our case, the radars and in situ probes are ~~in~~on the same platform and share a common GPS time server so their data are temporally synchronized. Temporal sampling rate of the post-processed triple-frequency radar data is 0.5 seconds (section 3.4a1.1). For particle probes, data are usually integrated over a period of 2-5 seconds ~~for~~to ensure their good quality; hence, the ~~radars~~radar data need to be decimated to match with the in situ measurements. On the other hand, there is a difference in sampling location between the radar and in situ. The nearest reliable NAWX and KPR radar data for triple-frequency analysis is 245 m above or below locations where in situ data were measured (section 3.4b1.2). Although the setup offers much higher accuracy in radar - in situ measurement coincidence compared to previous studies, it still brings in a question of how the radar data should be processed along the range axis to best characterize the microphysics. In order to answer that question, first, we need to examine the variability of DFRs in the range dimension. This is done using data from several flight segments during the RadSnowExp campaign.

3.3.1 DFR variability

The DFR variability studied in this section is defined as the fluctuation in DFR values along the radar range axis and will be analysed by comparing DFRs computed above and below the aircraft. Figure 75 shows examples of scatter plots of DFRs at the first usable distance (245 m) above and below the aircraft for all data points in a RadSnowExp flight on 22 November 2018. In the region of DFRs < 5 dB, the difference of DFRs ~~at~~in the two directions is often within 2-3 dB but for DFRs between 10 and 15 dB the difference can be as large as 8-10 dB.





335 **Figure 7- Scatter plot 5: Scatterplots of (a) DFR Ka/W (a) and (b) DFR X/Ka (b) of radar profiles at 245 m above and below the aircraft for all data points from a RadSnowExp flight on the 22 November 2018 flight. The data grid is 0.5 dB. The dashed black line is the 1:1 line. The solid black lines are the mean curve and the one standard deviation error bars.**

3.3.2 Data selection

340 The DFR variability study in the previous section shows that at a given time, reflectivity ratios between two frequencies could vary up to 8-10 dB within 490 m in altitude, i.e. between the 245 m profiles above and below the aircraft. Averaging radar data over multiple range gates around the in situ sampling might increase biases in DFR estimates; thus, in this study we just use measured DFRs nearest to the in situ sampling. The remaining question is which dataset, above or below the aircraft, should be selected. In order to assess how well the radar data would match the measured particle size distribution (PSD), [the](#) equivalent reflectivity factor at X-band is forward modelled from the measured composite PSD using the Rayleigh-[Gans](#) spheroidal approximation and Brown and Francis (1995) mass size relation. The X band is chosen because it is least affected by attenuation and non-Rayleigh scattering [effects](#). The simulated X-band reflectivity is then compared to the NAX radar data using the Pearson's correlation coefficient. Correlation coefficients using a 10 minute long running window are used to determine flight segments to be analysed. [Specifically, only](#) The 10 minute window is chosen to avoid the case where the cloud field is [homogenous](#) (i.e. the correlation would be close to 0) and to reduce the fine variation in the estimated correlations. At the [Convair's ground speed of 100 ms⁻¹](#), a 10 minute window corresponds to 60 km. [In the environment we flew \(this Arctic storm\), the likelihood of the cloud being homogeneous over a 60 km scale is utterly negligible. On the other hand, if a longer window is used the results will be smoothed out, possibly leading to an inaccurate selection. In this study, data points with correlation coefficients higher than a 0.6 threshold were selected in the analysis. This will ensure an accurate analysis of the are considered for triple-frequency radar analysis.](#) Illustrations of this procedure are given in [Fig. 10](#) [section 4](#).

355 **4 Triple-frequency case study: Arctic storm on 22 November 2018**

On 22 November 2018, the Convair-580 conducted a [3.5 hour](#) flight in the Canadian Arctic across the Frobisher [bay](#) area near Iqaluit. Spiral and lawnmower patterns were used for sampling at the outskirts of an Arctic storm which is clearly visible on the imagery from AVHRR sensor (channel 4, 10.3 μm) on board NOAA 13 polar orbiting meteorological satellite (Fig. [8a6a](#)). At the beginning of the flight, the aircraft climbed to 6 km and later descended to 1.7 km in steps- (Fig. [6b](#)). Next climb was in steps, to 2.9 km, followed by descent and landing (Fig. [8b6b](#)). In terms of cloud properties, mostly mixed-phase conditions were

observed, with moderate to heavy icing causing electrostatic discharges on the windshield in the second half of the flight. Diverse hydrometeor habits including rosettes, rosette-aggregates, and irregular shapes were sampled during the cruise at an altitude of ~6 km with in cloud temperature of -40 °C (Fig. 97) whereas pristine plates, capped columns, and densely rimed particles were observed at the lower altitude with temperature centered around -15 °C. Figure 97 shows the ground to air temperature and the distribution of the in situ temperature for the 22 November flight.

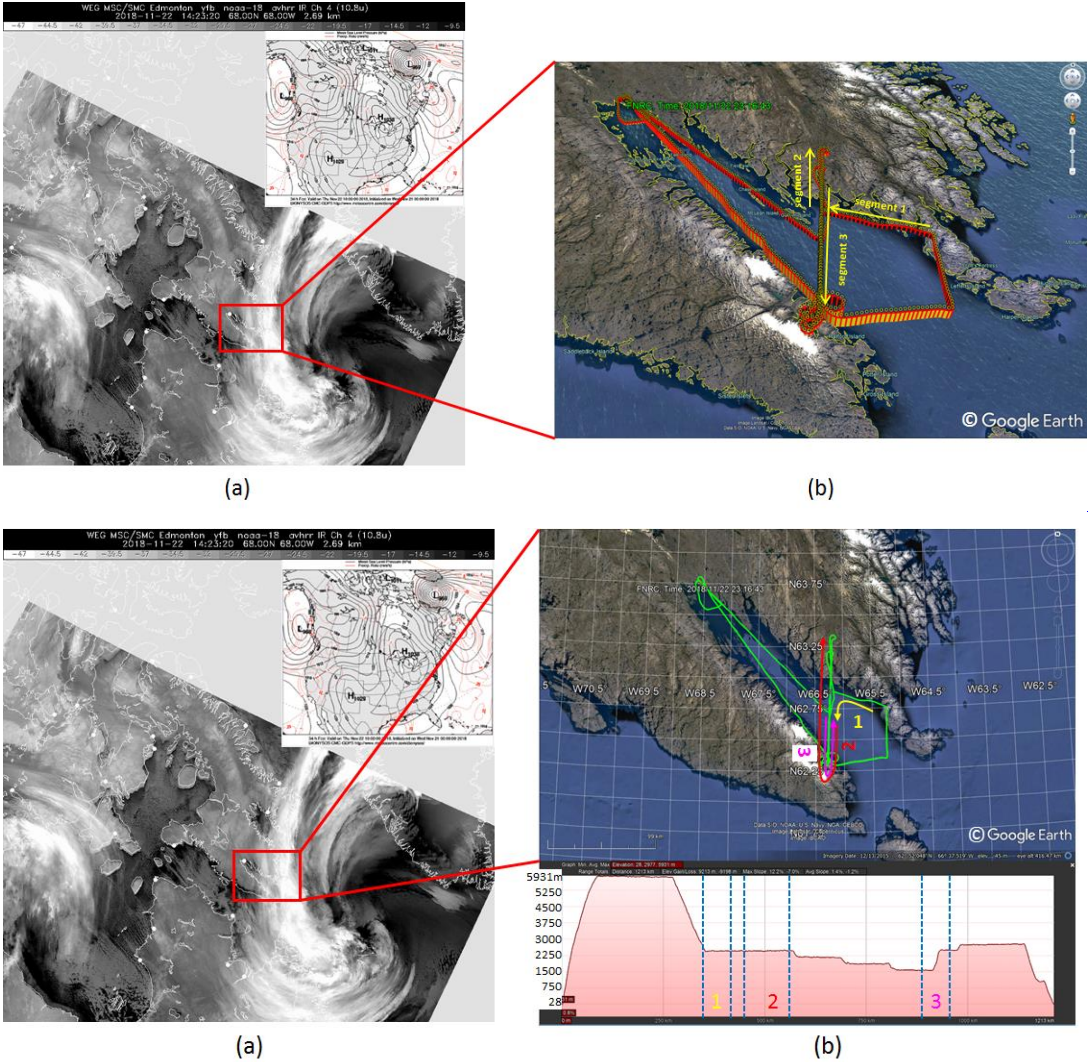
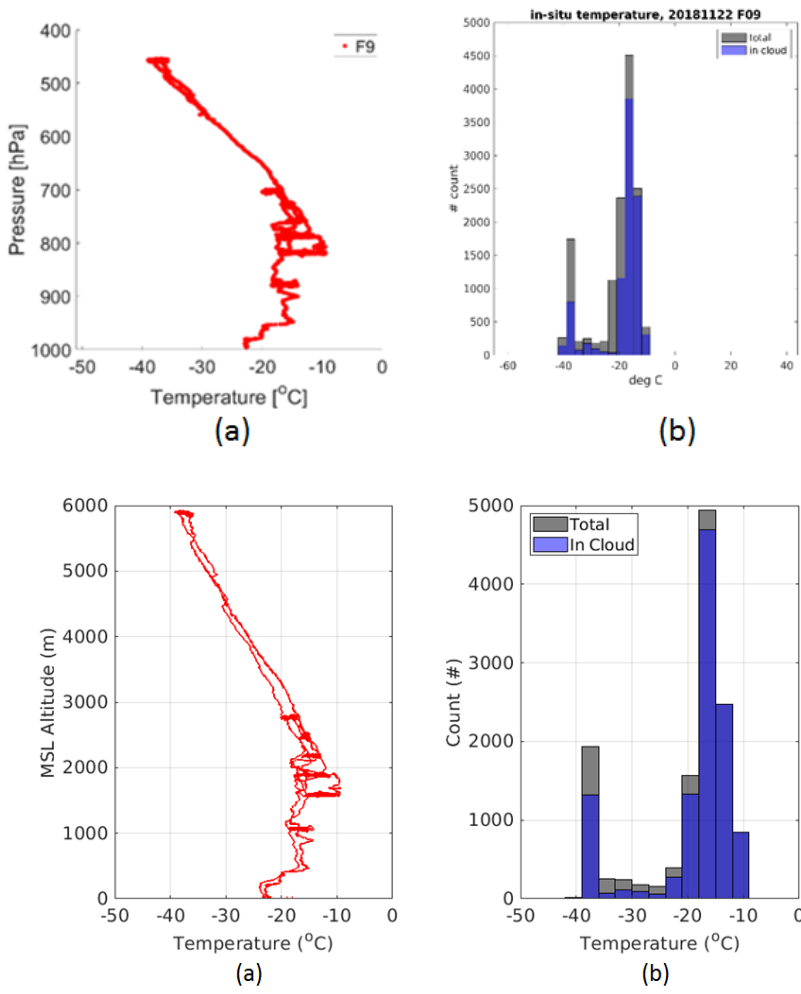
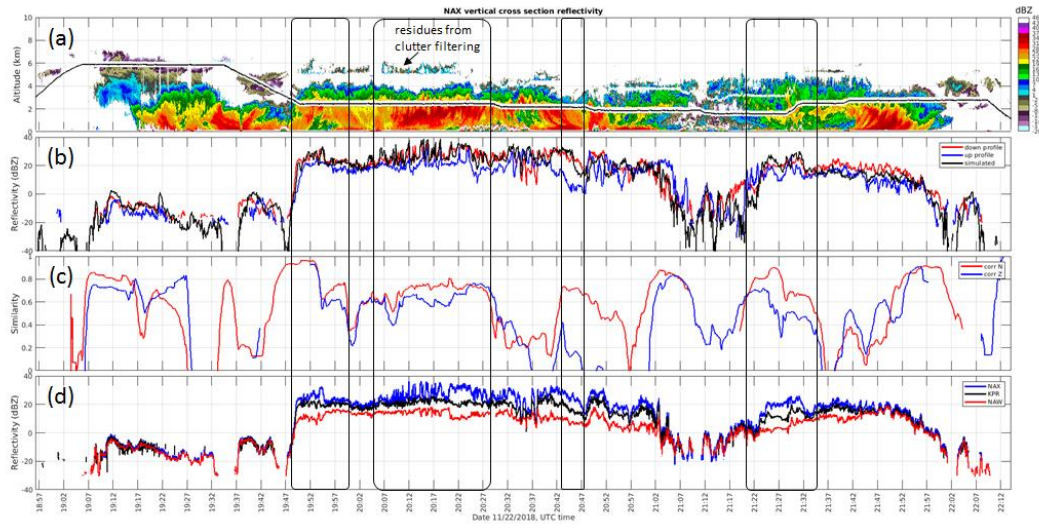


Figure 8-6: (a) NOAA-13 10.3 μm channel AVHRR imagery showing the Arctic storm—(a), and (b) the Convair flight track (green) and altitude plot on 22 November 2018—(b). Locations of three legs of this flight used for the case studies in this flight are indicated in (b) marked with different colors (yellow, red, and magenta).



375 **Figure 9:** During 7: (a) Temperature as a function of altitude for the 22 November flight, the ground to air temperature was in a range of $[-40^{\circ}\text{C}, -10^{\circ}\text{C}]$ (a). A temperature inversion was located at 1 km altitude. (b) Histogram of the in situ temperature (b) shows that for most of the flight the in cloud temperature was at around -15°C .



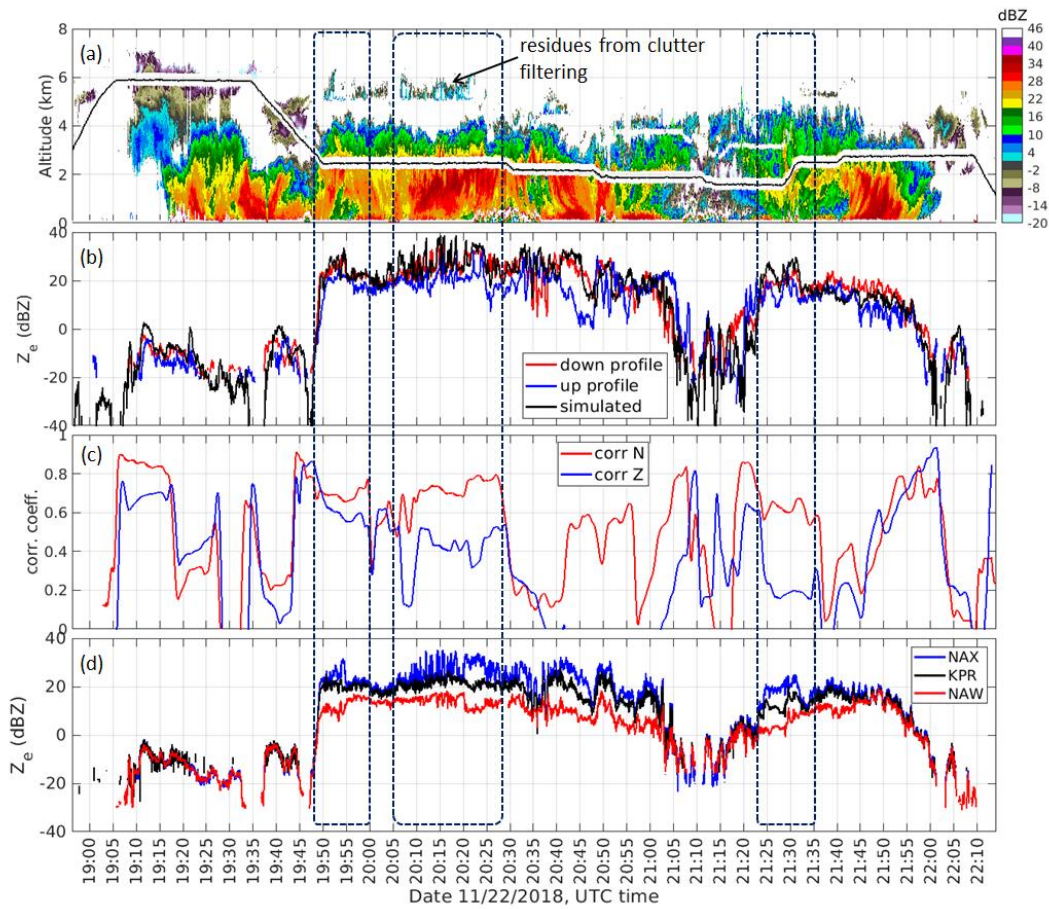


Figure 10e8: (a) X-band vertical cross section reflectivity for the flight on 22 November (a); flight; (b) reflectivity profiles at 245 m above and below the aircraft along with simulated X-band reflectivity reflectivities calculated from the measured PSD (b); similarity measurements (PSDs; (c) correlation coefficients) between the above/below Z-profile reflectivity and simulated Z-profile (c); reflectivity; (d) reflectivity profiles of X₂, Ka₂, and W₂ band radar at 245m below the aircraft showing the regions with interesting triple-frequency radar signatures (d). Boxes indicate the specific segments that will be analysed further.

In Fig. 10e8a, vertical cross section reflectivity at X-band of the entire flight is shown. The X-band data is selected to be representative of the radar reflectivity vertical structure of the storm as it is the least affected by attenuation and non-Rayleigh scattering. It is noted that there is a gap in the data at the up antenna of the X-band radar and some residues from the filtering of ground clutter leakages (Nguyen et al., 2024-2022). In addition to the radar time-height reflectivity cross section, radar reflectivity profiles at a distance of 245 m from the aircraft at up and down antennas are depicted along with simulated X-band reflectivity using the in situ PSD data (Fig. 8b). The probability density functions (pdf) of the X-band reflectivity at the nearest 245 m range above and below the aircraft are shown in Fig. 449. The pdf figures show that the aircraft stayed in inhomogeneous cloud layers (as highlighted by the difference between the nadir and zenith data with higher reflectivities typically occurring below the aircraft). The correlation coefficients between simulated and measured X-band reflectivities (section 3b) as functions of time, are shown in Fig. 10e8c. For this flight, data from the down antenna often have higher

correlation with the in situ data than data recorded at the up antenna. Radar data with correlation coefficients ≥ 0.6 would be considered to be a good match with the in situ data. In addition to the [similarity measurements](#), correlation coefficients, reflectivity values and DFRs are also used to select case studies. In this work, we focus on instances where non-Rayleigh scattering occurs as indicated by differences in radar reflectivity measured at the three frequencies (Fig. 40d8d). We have selected three different segments for further analysis of triple-frequency (indicated by [box 1, 2, and 4 in Fig. 10](#)), [boxes in Fig. 8](#)) giving a total number of 49 minutes of observations or 588 data points for analysis.

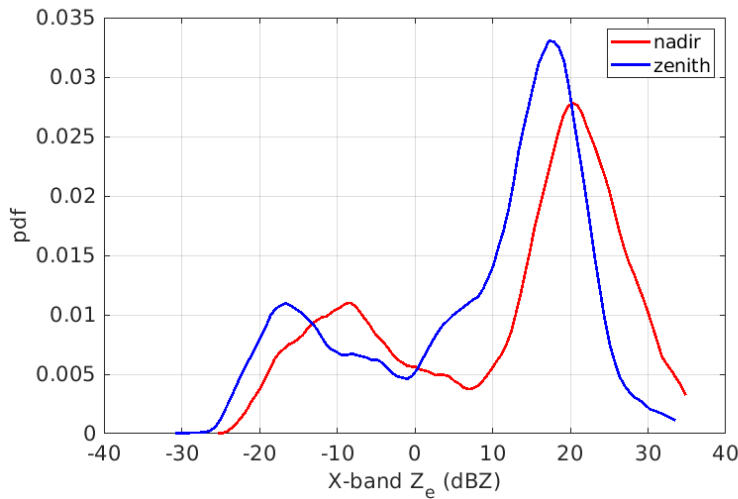
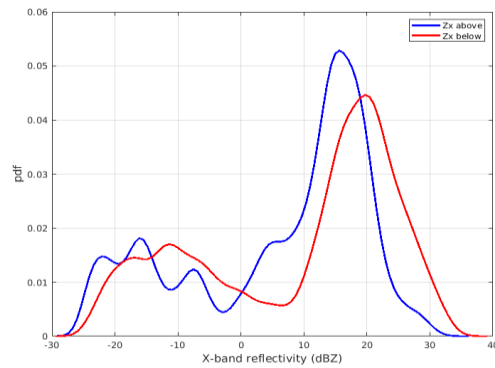


Figure 11: PDFs of the nearest range reflectivity X band reflectivities at 245 m above and below the aircraft for the 22 November 2018 flight.

4.1 Segment 1: 1948-2000 UTC

In this flight segment, the aircraft descended from 2.8 km to 2.4 km with [temperature](#) spanning the range of [-18, -15] °C. During the descent, the aircraft first sampled irregular shape ice crystals and small-ice in a mixed-phase environment with maximum size < 1 mm and then stayed at the same altitude sampling mixed phase clouds consisting of supercooled cloud drops of various sizes, rimed dendrites, pristine ice crystals and irregular types. The case is divided into five different sections (A-E) for detailed [triple-frequency](#) analysis based on dominant particle compositions that resulted in discernible DFR signatures.

In Fig. 10, panels (a)-(e) show the time series of the triple-frequency reflectivity, DFRs, PSD spectrum, MVD, ρ_e , TWC and LWC for this study case. Figure 10f shows the fractional composition of cloud particle types within the CPI detection range (<2 mm) of all major hydrometeor types over time (Table 2), and only the fractional composition of the ice subset is depicted in Fig. 10g. Also, in Fig 10g, a time series of the differential reflectivity from the side looking antenna of the X-band radar is shown. The average PSD (Fig. 10h) and mass distribution profiles (Fig. 10i) of the five sections selected for detailed triple-frequency analysis. The PSD and mass distributions are generally bi-modal with two ice modes around $30 \mu\text{m}$ and 1 mm . In Fig. 10j, representative images of single particles extracted from CPI and HVPS3 for each section are presented.

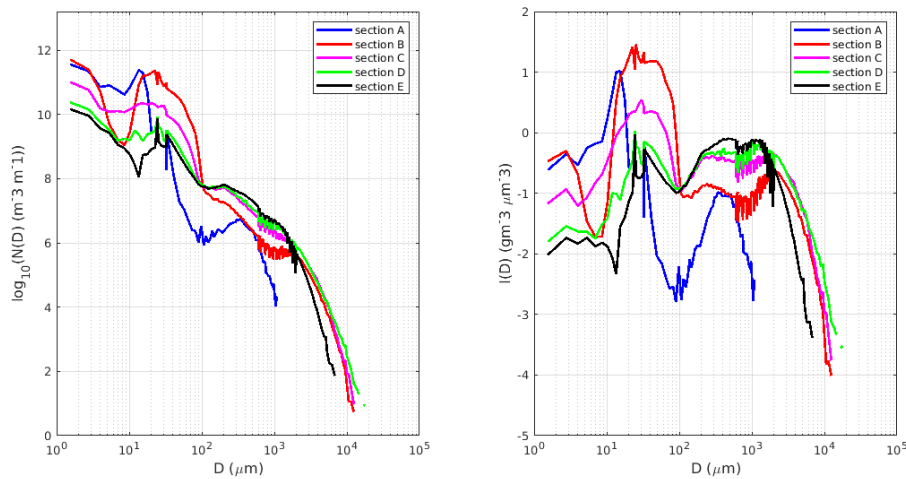


Figure 12: Averaged PSD (a) and spectral distribution of IWC (b) profiles for five sections selected in Fig. 12. The BF95 mass-size relationship was used to compute the IWC spectrum.

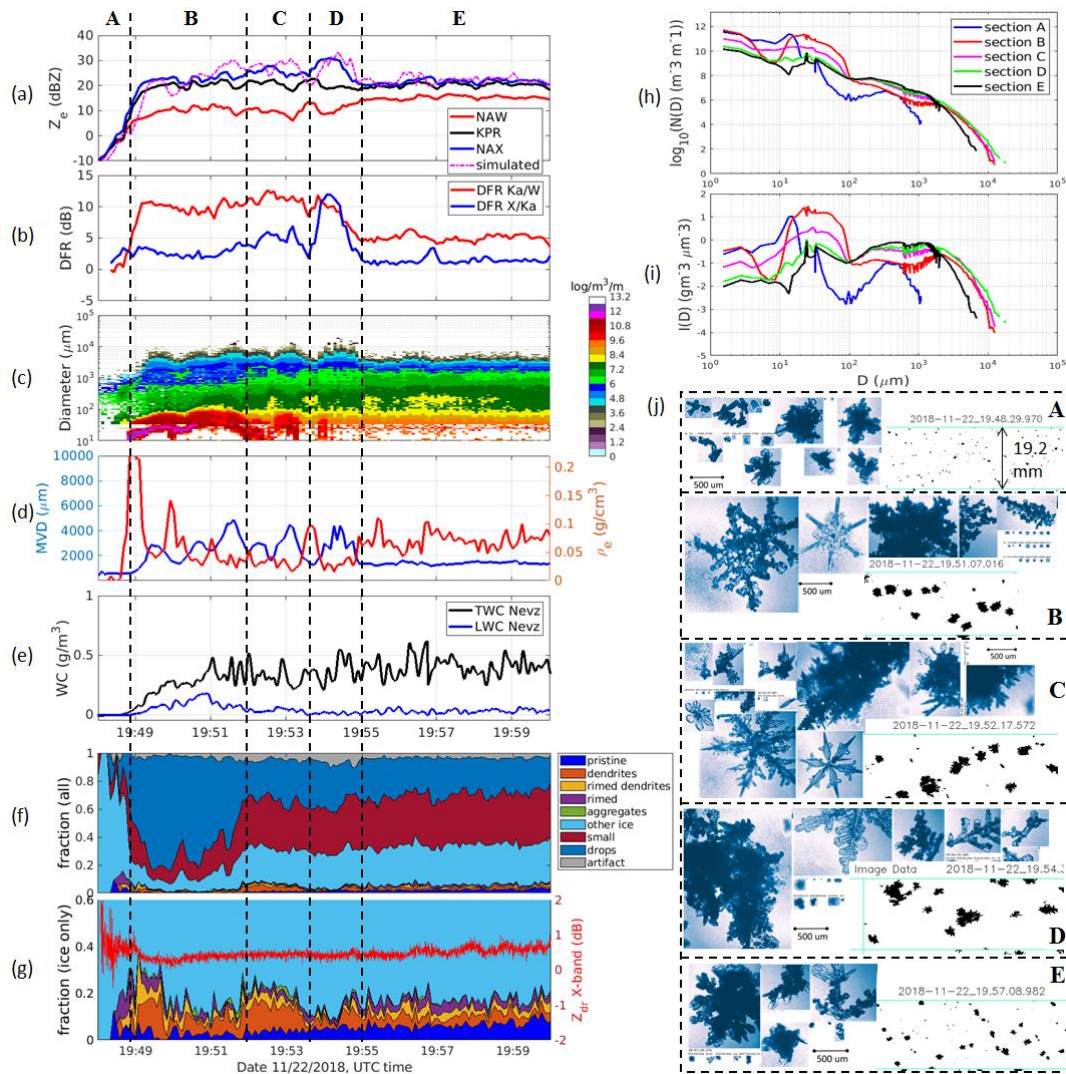
In Fig. 13, the left panels show time series of the triple frequency reflectivity, DFRs, PSD spectrum, MVD, IWC and LWC for this study case. The right panels show the fractional composition of cloud particle types within the CPI detection range (<2 mm) along with representative images of single particles extracted from CPI and HVPS3 for each flight section. In the CPI cloud composition plots, the top panel shows the fractional composition of all major hydrometeor types over time (Table 2), and in the middle panel, only the fractional composition of the ice subset is shown. In the first section (section A), during descent, the most common habits are irregular and small ice. The DFRs are ice with some densely rimed particles (Fig. 10j). DFR Ka/W is near 0 dB, in agreement with the small particle sizes shown in PSD and the CPI images, and DFR X/Ka in the [2, 4] dB interval. As the aircraft entered into mixed phase clouds at the start of section B at the altitude of 6.24 km , there was a significant increase in the number of drops and stellar dendrites with some heavily rimed dendritic fragments and graupel. Subsequently, bigger aggregates start to appear in the HVPS3 detection range. At around 19:51 UTC, the fraction of drops (Fig. 13, top right panel) increased to its maximum values, which is consistent with the LWC peak (up to 0.2 gm^{-3}) observed by the Nevzorov probe (Fig. 13, bottom left panel). With the presence of large particles (dendrites, and rimed particles), the DFR values sharply increased to $\sim 10 \text{ dB}$ (Ka/W) and $\sim 4 \text{ dB}$ (X/Ka). There are some DFR variabilities in this section due to changes in PSD and particle composition. For example the slight decrease in DFR values around the middle of section B (around 19:54:30 UTC) remarkably mirrors/resembles the decrease in the relative concentrations of dendrites and rimed particles (Fig. 13, middle right panel). Section C is from sampling of the storm when the aircraft descended to 1.7 km and sampled flew in clouds with

440
445
450
455

some heavily rimed dendrites, large aggregates as observed by the HVPS3 probe and a reduced (Fig. 10j). The fraction of number rimed dendrite, unrimed dendrites, and large aggregates increases and the fraction of small drops by the CPI probe decreases compared to the second half of section B. It is worth to note that in sections C-E, the percentage of pristine, small particle and drop categories are relatively constant. In this section, the DFRs slightly rise, which is consistent with an increase in dendrites portion within the proportion of dendritic ice habits (middle panel in Fig. 4310g) with some of them heavily rimed. In section D, mainly heavily rimed, fractured ice and frozen drops are present with bigger aggregates detected by HVPS3 (Fig. 10j). The DFR X/Ka reaches its highest value (~13 dB) exceeding the corresponding DFR Ka/W. Interestingly, this section contains large dendrites with heavy riming and the PSD profile is broader and flatter compared to that of section B-C (Fig. 4210i). It also shows a slight increase in the larger sizes whilst the fraction of dendrites and rimed particles drops to its lowest level: at the first half of the section when the highest DFR X/Ka occurs. Lastly, in section E, an increase in the number of smaller particles in pristine shapes like plates, rimed dendrites, frozen drops and also smaller aggregates were detected with the HVPS3. The bulk density is also higher in this section and the MVD from PSDs are also remarkably stable at about 1.6 mm. The DFR X/Ka and Ka/W are fairly constant around 21.5 dB and 5 dB, respectively. The reduced DFR values are consistent with a decrease in maximum particle size (Fig. 42a10h). The small variations in DFR values also agree well with the relatively uniform fraction of cloud particles depicted in the CPI frequency plots (Fig. 10g). In section A, the X band horizontal Z_{dr} is noisy due to weak returned signal but in section B - D it is clean, remains fairly constant at about 0.5 dB. In section E, Z_{dr} slightly increases to 0.6-0.8 dB and this enhancement in Z_{dr} is consistent with the increase in riming level which is indicated by the higher bulk density and TWC in this section (Li et al., 2018).

The figure consists of two main columns of plots. The left column shows radar and probe data over time (Date: 11/22/2018, UTC time). The top plot is Reflectivity (dBZ) from -10 to 40. Below it is DFR (dB) from -5 to 15. The third plot is $\log_{10}(N)$ (m⁻³) from 10⁰ to 10³. The fourth plot is MVD (µm) from 0 to 8000. The bottom plot is WVC (g m⁻³) from 0 to 0.8. The right column shows CPI particle fraction from 0 to 1.0 and HVPS3 images for sections A (19:48), B (19:51), C (19:53), D (19:54), and E (19:57). A legend on the right identifies particle types: pristine (blue), dendrites (orange), rimed dendrites (green), rimed (red), aggregates (purple), other ice (brown), small (grey), drops (black), and unfrozen (white).

22



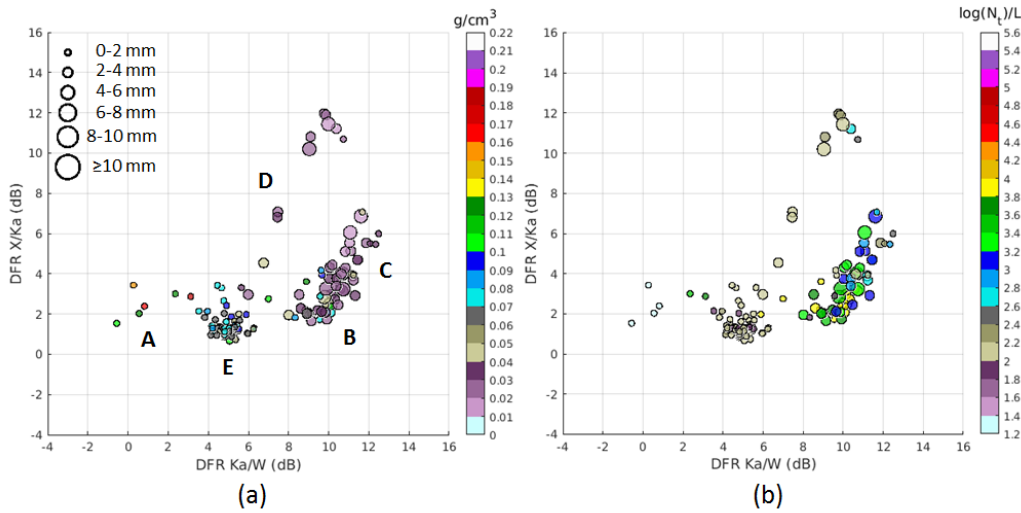
460 **Figure 13:** Left panels from top to bottom: (a) Segment 1948-2000 UTC in the 22 November flight; (a) triple-frequency reflectivity profiles; (b) DFR X/Ka and DFR Ka/W; (c) PSD spectrum; (d) characteristic diameters (MVD) and effective bulk density (ρ_e); and (e) TWC/LWC from Nevzorov probe for segment 1948-2000 UTC in flight 22 November 2018. Right panels from top to bottom: (f) fractional distribution of all hydrometeors detected with the CPI probes; (e) fractional distribution only of ice habits; (h) averaged PSD profiles; (i) averaged spectral distribution of IWC; and (j) representative images from CPI (blue) and lower resolution images of large hydrometeors from HVPS3 (black) for each flight section (A, B, C, D, and E). The width of the HVPS3 image strip is 19.2 mm. The BF95 mass-size relationship was used to compute the IWC spectrum.

465

To characterize ρ_e , MVD and total concentration (N_t) in the DFR plane, the data are presented in Fig. 13 in such a way that each dot represents a data point, the size of the dot being proportional to the MVD with the color corresponding to ρ_e or N_t . It can be seen that the DFR values in the five sections (Fig. 13(b)) populate different zones in the DFR plane associated with unique scattering properties of different ice habits. In general, DFRs increase with increasing coincident MVD and DFR X/Ka decreases when bulk density increases. There are only few data points in section A (DFR Ka/W ~ 0 dB and 2 dB < DFR X/Ka <

470

4 dB, Fig. 10a) locating in regions predicted by modelling of triple-frequency signatures of bullet rosettes (Fig. 1). In section B and C where the strength of riming occurs, numbers increases, the number of concentration are significantly higher than other regions. The location of data from section B and C data-placement in the triple-frequency plane agrees well with scattering computations of graupel particles using discrete dipole approximation (Fig. 6 in Tyynela and Chandrasekar (2014)). Section D is particularly interesting because of the PSD composition and only aggregate models (Tyynela and Chandrasekar (2014), Kneifel et al., Leinonen, J. and Szyrmer, 2015; Stein et al., 2015; Ori et al., 2020) are comparable with the “hook signature” observed observation in the data points. (Fig. 11d). The distribution of the data points in this section appears as nearly a vertical curve which could be attributed to its broader PSD (Mason et al., 2019). In this case, we observed large dendritic aggregates with heavily riming clouds only a small proportion of rimed cloud particles. Compared to section C (which overlaps with the scattering computations for spheroid models as in Leinonen et al. (2012)), the total concentration of the data points in section D was much lower (Fig. 11e and 11f) whilst the TWC was larger. (Fig. 10e). The data in section E are characterized by higher bulk density values with MVD in the [0, 2] mm interval and are located in a region which overlaps with the modelling results for small aggregates and graupel (Fig. 2).



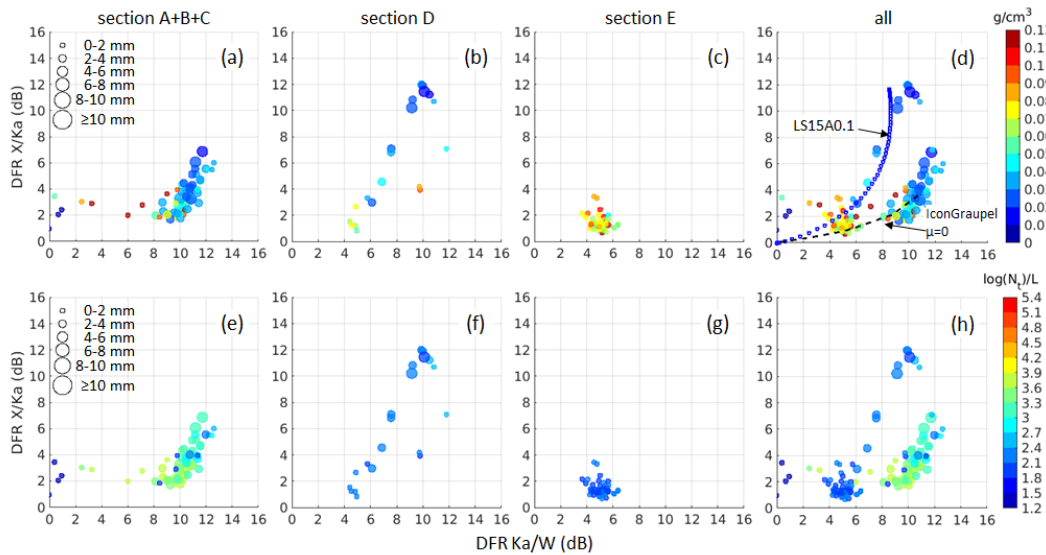


Figure 141: DFR scatter plots for the 1938-2000 UTC segment, in the November 22 flight. Data points are coloured by the effective bulk density (ρ_e) (a-d) and by the total concentration (N_t) (e-h). The dot size is proportional to the calculated MVD. The letters (In panel (d), the blue line is for riming model A-E) indicates each flight section as in with effective liquid water path of 0.1 kg m^{-2} (Leinonen and Sztymer, 2015) and the black line is for a graupel model from Fig. 13-2.

4.2 Segment 2: 2005-2028 UTC

In this case, the aircraft maintained the altitude of 4.724 km (Fig. 10a), but penetrated regions inland from Frobisher Bay (Fig. 86). The segment is divided into three sections (A-C) (Fig. 4612) for a detailed analysis. This is still a mixed-phase environment with pockets of high concentration of drops (with diameter of approximately $30 \mu\text{m}$) and an ice mode at $\sim 1.5 \text{ mm}$ (Fig. 45-12i). Different ice habits such as pristine particles, dendrites, fractions of dendritic aggregates, and rimed particles were observed and shown in samples of CPI imagery (bottom right panels, Fig. 46-12j). Larger aggregates (up to 10 mm) were also seen on HVPS3 black shadow images (Fig. 4612j). It is worth noting that the particle types observed in the three sections are the same. However, the level of riming and the fraction of dendrites and aggregates within clouds are different between the sections.

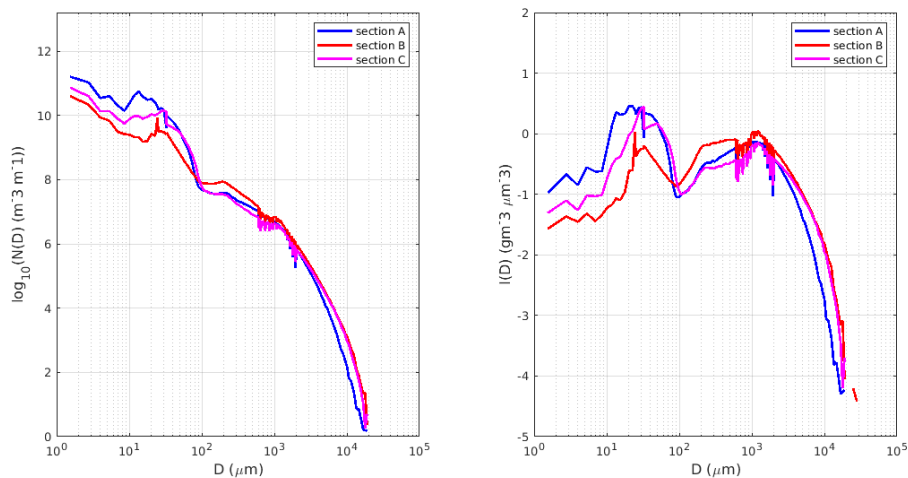
In section B, the fraction of rimed particles and dendrites (both pristine and rimed) is the highest. The highest TWC ($\sim 1 \text{ g m}^{-3}$) of the flight was also recorded in section B. During this section, the X-band radar reflectivity increased in-land with a number of high reflectivity cores at flight level (Fig. 40, second panel 8a), which is consistent with the high TWC (Fig. 12e) and higher relative concentrations of rimed particles and dendrites in the CPI frequency plot. (Fig. 12g). In section C, pockets of high TWC were also observed and the fraction of dendrites and rimed particles remains high with an increase of the relative portion of pristine dendrites and aggregates (Fig. 46, middle panel)-12g).

The fluctuation in the time series of the observed DFRs matches very well with that of the cloud particle mean diameters (Fig. 46, left panels 12d). It is also consistent with the fraction of rimed particles, dendrites, and aggregates (shown in the CPI composition plot, Fig. 4612g). In section A, mean values of DFR X/Ka and DFR Ka/W are $\sim 2 \text{ dB}$ and $\sim 6 \text{ dB}$ respectively with $21.5 \text{ mm} < MVD < 4.5 \text{ mm}$, respectively and DFR X/Ka - at times reached the same level as DFR Ka/W at around 8 dB for larger when MVD (\leftarrow is greater than 4 mm). Also, in section A, side-looking Z_{dr} fluctuates and, at points, reaches up to exceeding 1.5 dB which we suspect to be a result of dendritic particles/needle aggregates dominating the radar measurements.

In section B, the DFRs show high variability, mimicking/resembling the MVD changes and peaked at $\sim 10 \text{ dB}$ for both DFR X/Ka

and DFR Ka/W when the TWC is greater than 0.68 g m^{-3} and MVD is greater than $86 \text{ }\mu\text{m}$. The decrease in Z_{dr} in this section is consistent with higher degree of riming (Li et al., 2018). In region C, the DFR values remain high with the DFR X/Ka reaching over 12 dB. In section B and C, with the increasing number of large spheroidal compact aggregates due to riming, Z_{dr} is stable at $\sim 0.5 \text{ dB}$.

Distribution of all the data points in this segment in the DFR plane is shown in Fig. 17. Due to a large fluctuation variation in the DFRs, there are overlapping data points between the sections. Section A is characterized by the presence of small particles; hence it is mainly populated by relatively smaller dots with higher effective bulk density at 1.2 g/cm^3 (Fig. 13a). Data points in section B, where the fraction of riming particles reaches its highest value (Fig. 12g), overlap with both section A and C. Data points also, in this section B and C overlap but in section B, where the fraction of riming particles reaches its highest value (Fig. 16, left panel), the PSD is flatter (Fig. 15b) and the concentration of small drops is lower (Fig. 15a, 12h). In this segment section C, the fractions of dendrites and large aggregates increase whilst the fraction of pristine ice crystals drops from the previous two sections. In this case study, the location of all the data points shows a very clear illustration of the “hook signature”, i.e. the DFR Ka/W values decrease whilst the DFR X/Ka continually increases. Modelling results show a hook signature in triple frequency space from dendritic and needle aggregates (Petty and Huang, 2010), and snow aggregates composed of a variety of different primary crystal habits (Tyynela and Chandrasekar (2014), Leinonen and Moisseev (2015)) which agree with our in situ observations. Triple frequency lines for a riming model where aggregation and riming are undergoing simultaneously in a population of ice crystals (Leinonen and Szyrmer, 2015) are superimpose in the DFR plane. Two scenarios with different levels of riming (e.g. with fixed effective liquid water path of 0.1 kg m^{-2} and 0.5 kg m^{-2}) are shown (Fig. 13d). The modelling results agree with our measurements quite well although they do not capture the hook signature of the data. This indicates that the amount of riming varied significantly in this flight segment.



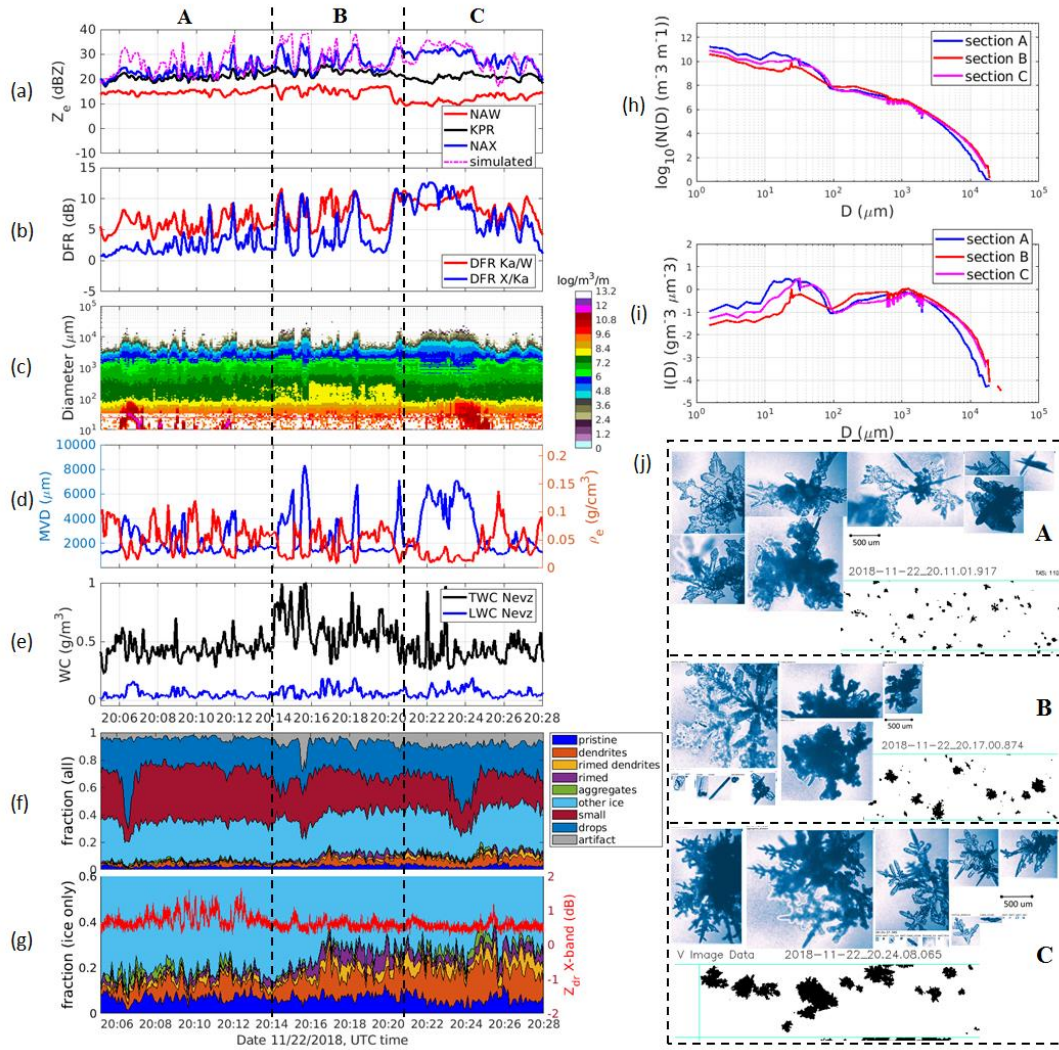


Figure 15: Averaged PSD (a) and mass distribution (b) profiles for three sections (A-C) selected in Fig. 15.

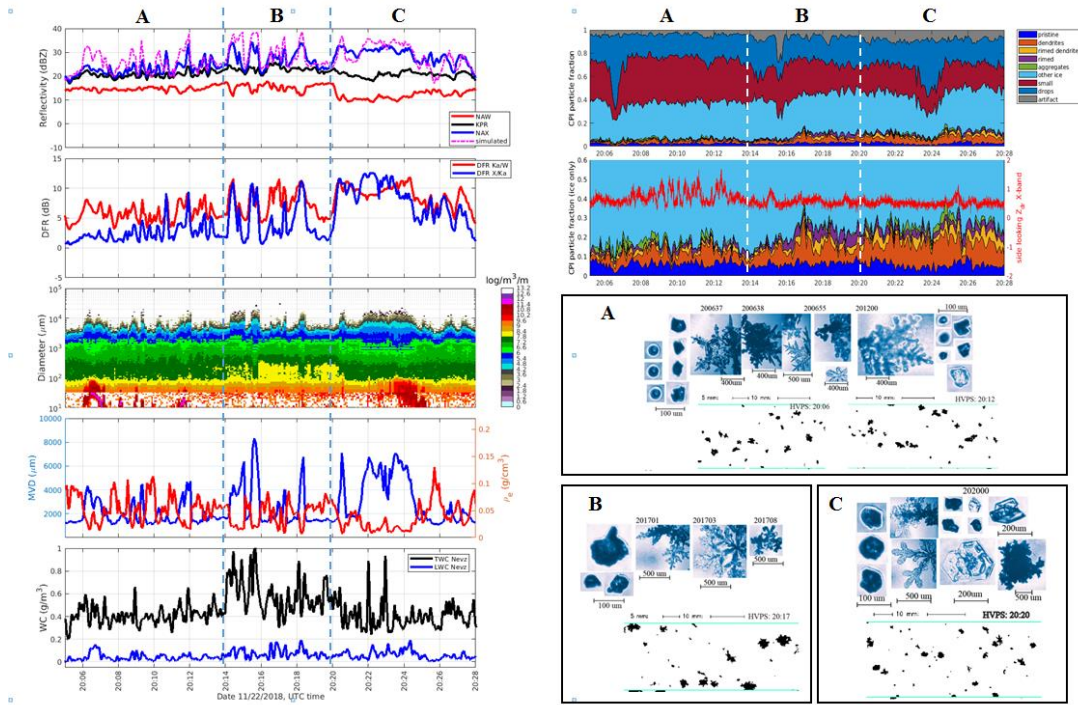
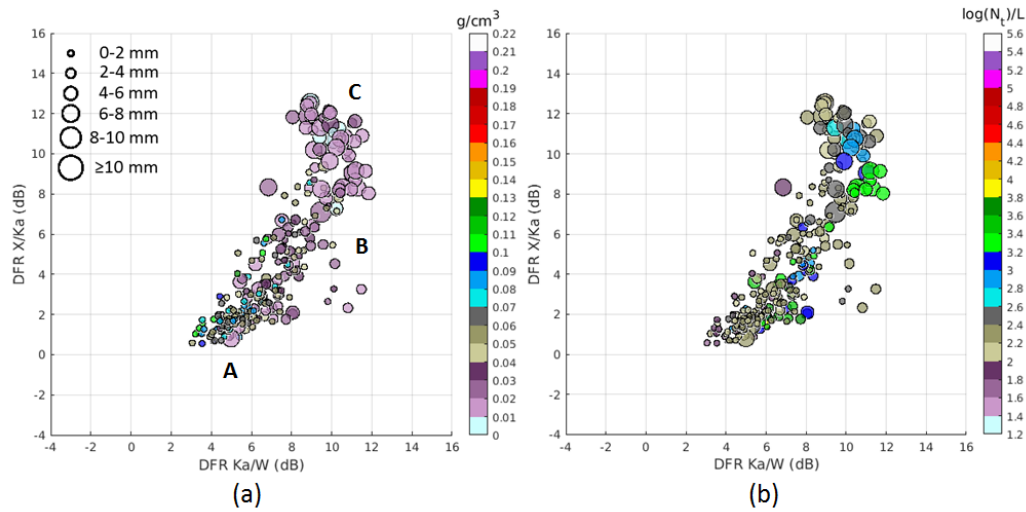


Figure 1612: Similar to Fig. 1210 but for flight segment 20:05 UTC – 20:28 UTC.



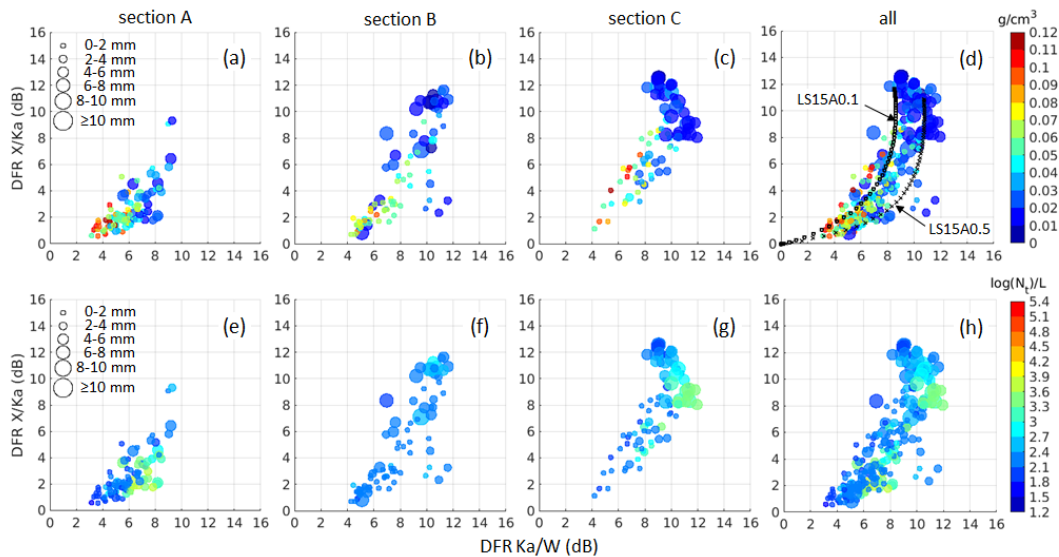


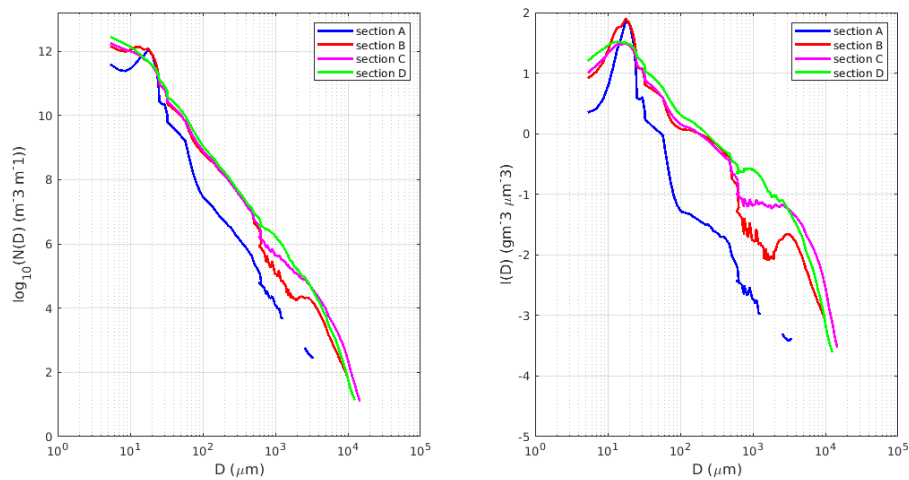
Figure 4713: Similar to Fig. 4411 but for flight segment 20:05 UTC – 20:28 UTC. In panel (d), the black lines are for riming model A with effective liquid water path of 0.1 kg m^{-2} and 0.5 kg m^{-2} (Leinonen and Szvrmer, 2015).

4.3 Segment 3: 2121-2135 212230-213500 UTC

545 For this case the aircraft sampled the precipitation system at a lower altitude of 1.76 km (Fig. 10) and then climbed up to 2.25 km at the end of the segment (Fig. 6). During this segment there was heavy ice accretion on the aircraft with subsequent electrostatic discharges on the windshield. The X band Z_{dr} is stable within [0.4, 0.8] dB indicating that the radar signals are dominated by spheroidal particles. The segment is divided into four subsections (A-D) based on the DFRs and cloud property signatures (Fig. 19). Section A consisted mainly of supercooled liquid droplets with LWC of $\sim 0.2 \text{ g/m}^3$ with a small fraction of sector plates and heavily rimed (<2 mm) particles (middle-left panels of Fig. 4914). DFR X/Ka and Ka/W are, in general, around 2 dB 2 dB which is consistent with this type of cloud particles. Effective bulk density and concentration are also at their highest values, $\sim 0.8 - 0.9 \text{ g/cm}^3$ and $\sim 10^{4.5}$, respectively. In section B, supercooled liquid droplets and small ice still dominated but started decreasing while millimetric rimed aggregates with the main mode at $\sim \text{MVD} \sim 3 \text{ mm}$ (Fig. 18b) appear. Both DFRs increase when the MVD increases with DFR Ka/W filling in the entire range from 2-10 dB and DFR X/Ka reaching up to 5 dB. The scatterplot of DFR X/Ka versus DFR Ka/W for these two sections is rather linear and can be characterized by simple spheroid scattering models (Leinonen et al., 2012). In section C, more dendrites and large aggregates with maximum size exceeding 10mm are found. At the beginning of this section (until 21:27 UTC), DFR Ka/W mirrors the change in MVD. DFR Ka/W goes up to 10-12 dB at $\text{MVD} \sim 6 \text{ mm}$ which is similar to the case of section C in the segment study case 2. However, DFR X/Ka is much lower at 5-7 dB. Moreover, after reaching its highest values ($\sim 12 \text{ dB}$), DFR Ka/W starts decreasing whilst DFR X/Ka continually increases and DFR X/Ka exceeds DFR Ka/W at $\sim 21:27 \text{ UTC}$. Visual analysis of the CPI images reveals the presence of aggregates of rimed dendrites with lower density (Fig. 4914j) during this period. Also, the PSD in this section is also broader and flatter (Fig. 4914i) which affects the distribution in the triple-frequency plane. (i.e. the data points locate in an almost vertical line). After 21:27 UTC, DFR Ka/W decreases whilst DFR X/Ka continually increases thus creating a clear hook signature create a turning point at $\text{DFR Ka/W} \sim \text{DFR X/Ka} \sim 8 \text{ dB}$ (Fig. 2015d).
 565 The location of the triple frequency data in this section overlaps with a region where different snowflake aggregation models

exists (Fig. 2). For example, modelling results for an aggregation model described in Kuo et al., 2016 agree reasonably well with the DFR values and patterns agree well with modelling results for aggregate of fernlike dendrites (Tyynela and Chandrasekar, 2014). In fact, the fraction of dendrites in this period is noticeably higher than that at the beginning of the section (top right panel, Fig. 19) in this section.

570 In the last section (D), where the aircraft ascended from 1.76 km to 2.95 km, the fraction of dendrites rimed particles and aggregates with MVD ~ 1mm increased at the first half of the section. The bulk density in section D is higher compared to other sections (left panel, Fig. 1914d) consistent with heavily rimed clouds identified from the CPI probe. Both DFRs start decreasing which mirrors similar to a decrease behaviour in MVD and become comparable at around 3-4 dB. The DFR scatterplot for this section, similar to the study case 2, is in a great agreement with a riming model described in Leionen and Szyrmer, 2015 (Fig. 575 15c). Data from all four sections are plotted in Fig. 15d and 15h showing a clear hook signature. It is also worth noticing that the concentration in this cloud segment is much higher than in the previous two cases.



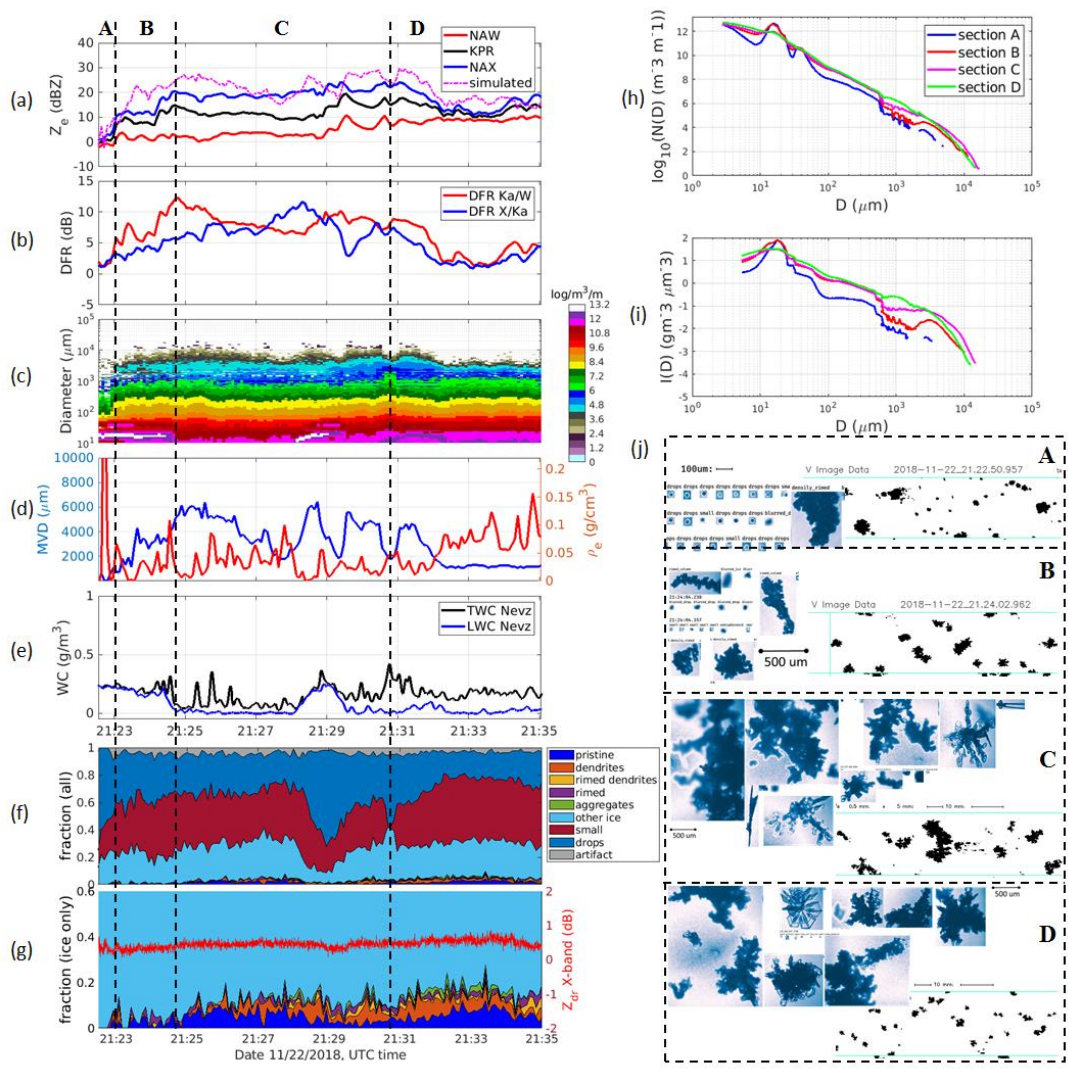


Figure 18: Averaged PSD (a) and mass distribution (b) profiles for four sections (A-D) selected in the Fig. 19.

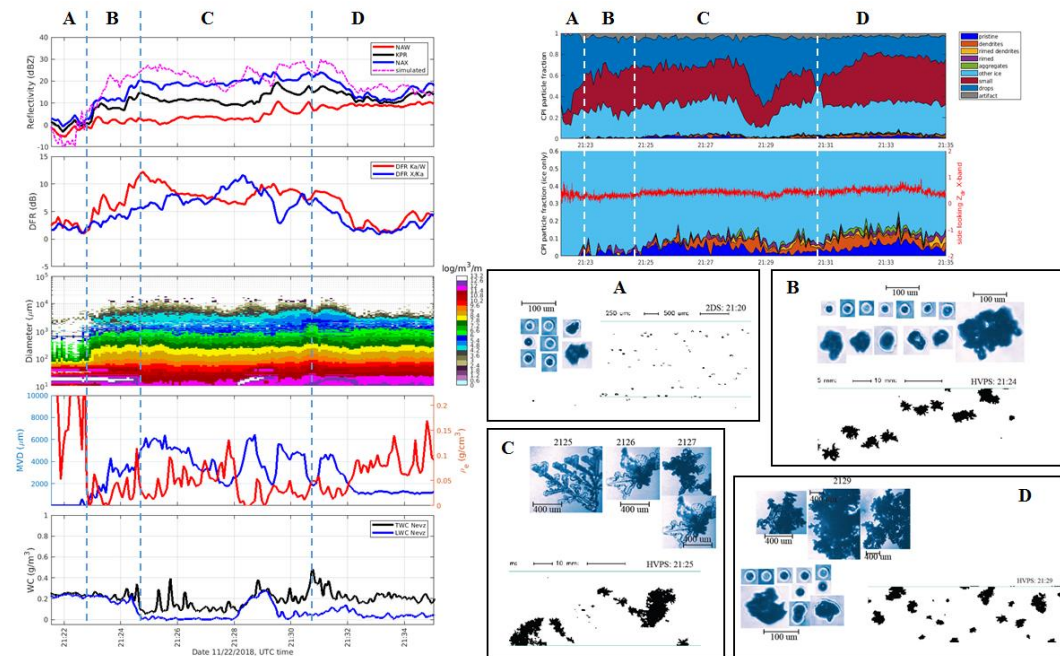
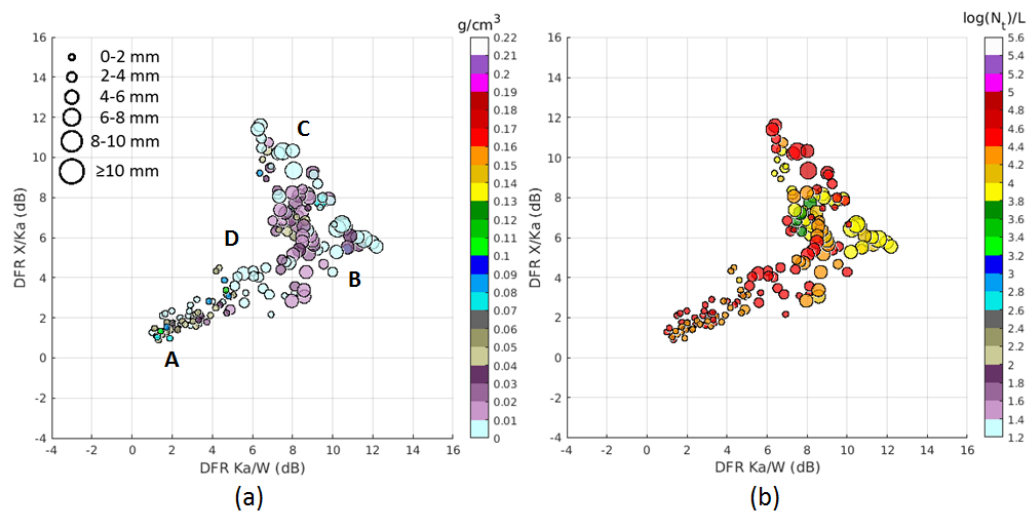


Figure 1914: Similar to Fig. 12 but for segment 21:21:22:30 UTC – 21:35 UTC.



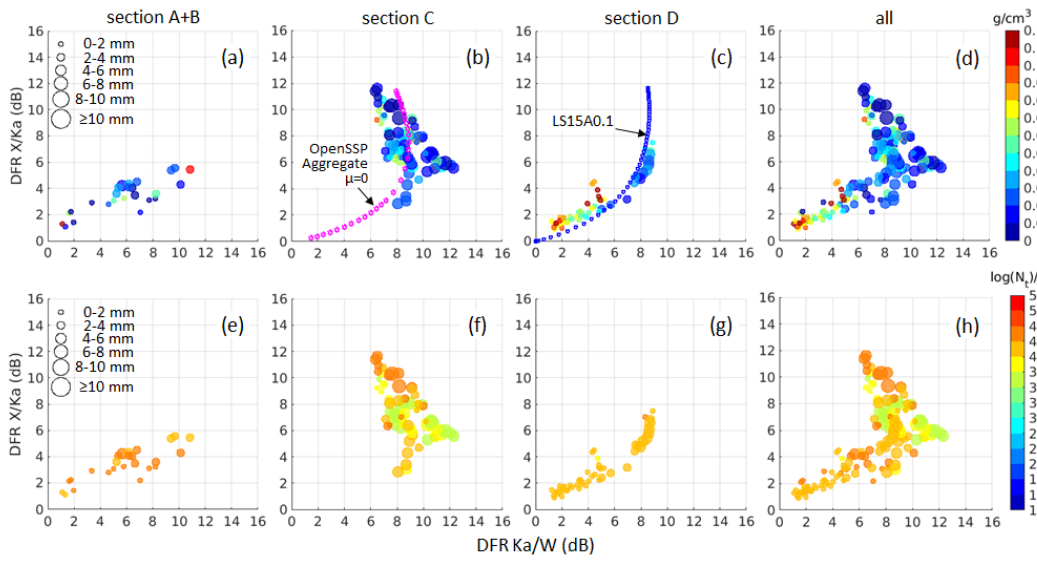
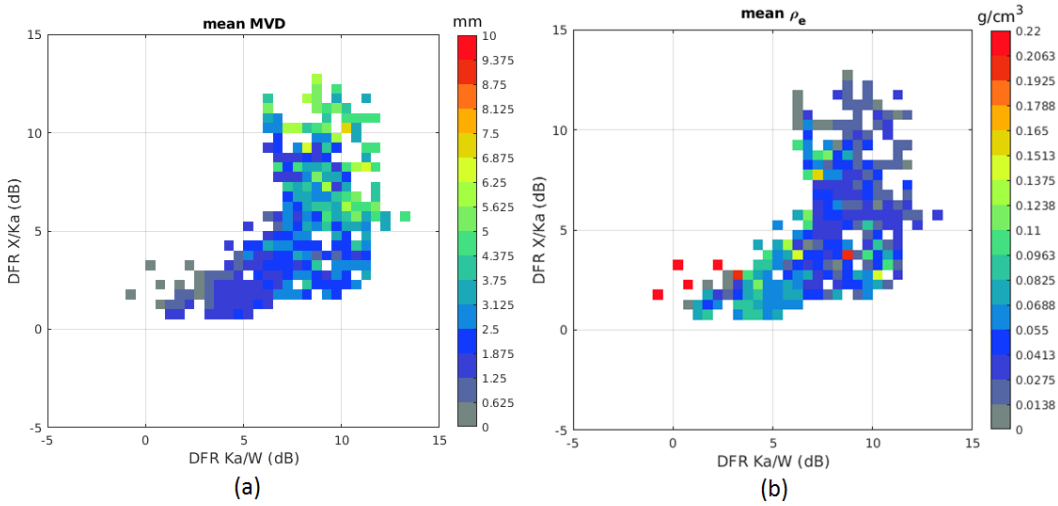


Figure 2015: Similar to Fig. 14 but for flight segment 20:05 UTC – 20:28 UTC. The magenta line (in panel (b)) is for the aggregation scattering model (Kuo et al., 2016) and the blue line (in panel (c)) is for riming model A with effective liquid water path of 0.1 kg m^{-2} (Leinonen and Szyrmer, 2015)



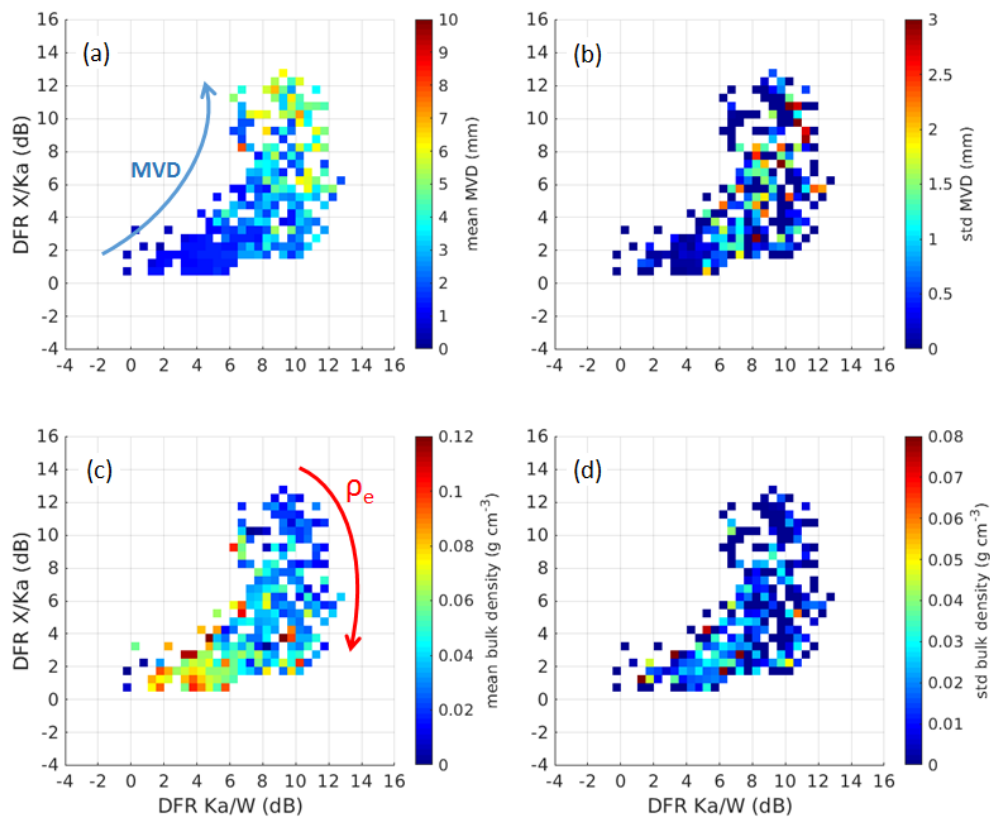


Figure 24:16: (a) Mean MVD; (b) standard deviation (std) of MVD; (c) mean ρ_e ; and (d) std of ρ_e calculated from all the data points (573 samples) analysed in three study cases in of the 22 November flight on November 22nd, 2018. The data are binned onto a grid with grid size of 0.5 dB in both axes. The mean and standard deviation are computed from the data within the bin.

Formatted: Font: 10 pt, Not Bold

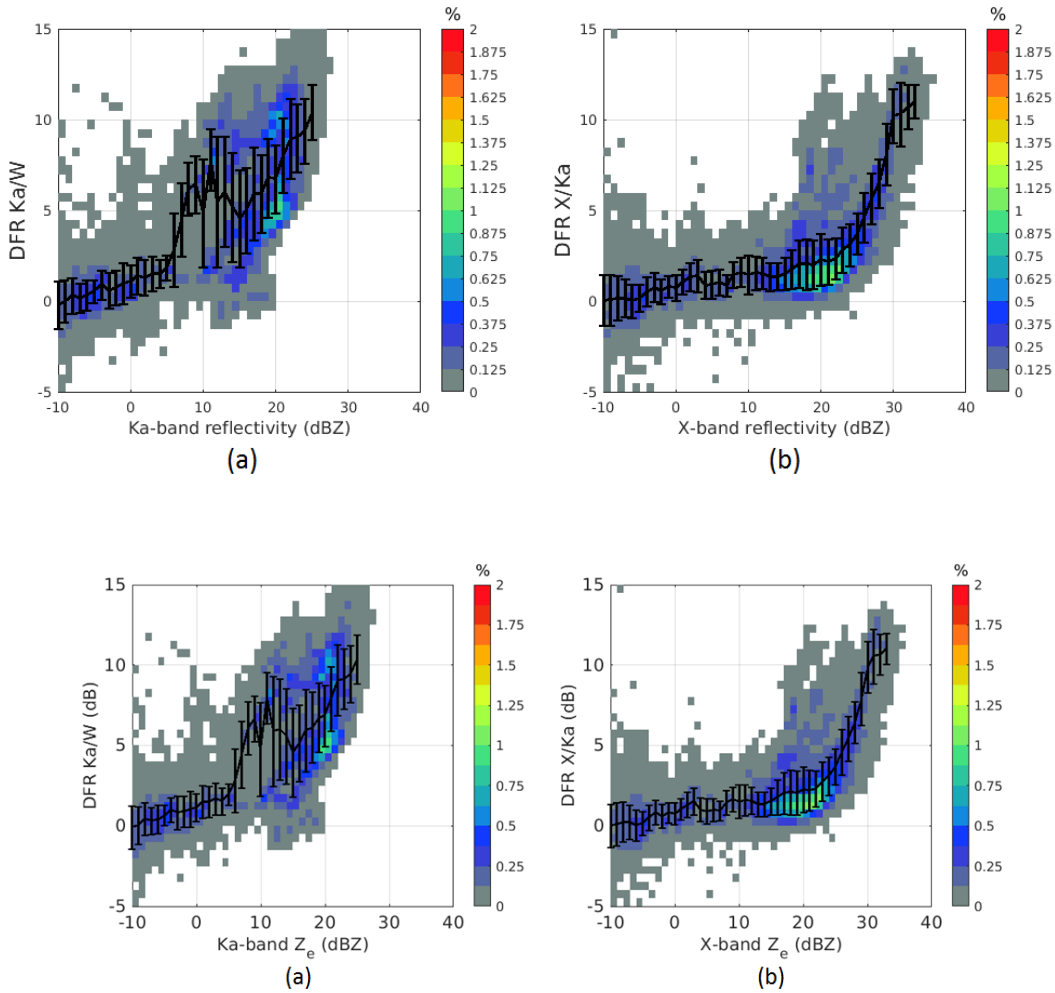


Figure 2217: Occurrence density plot of (a) Ka-band reflectivity vs. DFR Ka/W (a) and (b) X-band reflectivity vs. DFR X/Ka (b). Data are from () using nadir antennas in the 22 November 2018 flight (Fig. 9) with data (over 23500 data points,) from the 22 November flight. The black lines present means and error bars (one standard deviation) of the DFRs.

5 Summary and discussion

The X-Ka-W-band airborne radar observations and almost perfectly co-located in situ microphysical measurements collected during the RadSnowExp project provides provide an unprecedented dataset for radar studying multi-frequency study radar signatures of snow/ice clouds. The whole RadSnowExp dataset includes more than 12 hours of dataflight data in mixed phased and glaciated clouds with more than 3.4 hours in-when the scattering was non-Rayleigh regions-for at least one of the radar frequencies. The-potential-In this study, we careful selected three different flight segments with well-matched airborne in situ and

610 ~~radar measurements of this dataset is illustrated here using one flight data during an a winter storm in Arctic storm that covers a wide range of snow habits from low pristine ice crystals, low density aggregates region to heavily rimed particles with maximum size exceeding 10 mm. The analyse~~ triple-frequency ~~signals~~ signatures of various hydrometeor compositions. The dual-frequency ratios (DFRs) in three study cases are observed as large as 12 dB, and they appear to be ~~determined~~ dominated by non-Rayleigh effects ~~only thanks to the close range measurements and additional processing which improve radar volume matching~~. The study cases were observed in a relatively large temperature range between -40 and -10 °C and at different flight altitudes.

~~In this work, we focus~~ Efforts were directed on finding the relationships between ice particle properties and radar triple-frequency ~~signatures~~ observations and their potential for developing quantitative retrievals of fundamental ice cloud microphysics. We also ~~provides~~ provide brief discussions on some measurement aspects (DFR variability and radar sensitivity) which might affect the triple-frequency radar applications. ~~Preliminary results~~

615 ~~The result from our study~~ confirm the main findings of previous modelling works with radar ~~dual frequency ratios (DFRs)~~ moving within different zones of the DFR plane (Leinonen et al. (Leinonen et al., 2012), Kulie et al. (Kulie et al., 2014)). We find that the size of the crystals has a measurable effect on the triple-frequency signals. The ~~mean~~ particle diameter increases further from the origin of the DFR plane, with increasing DFR values corresponding to increasing MVD. The ~~signal of the~~ DFR X/Ka and the DFR Ka/W pairs respond to different particle size ranges, with more linear responses for MVD ranges of 2-408 mm and 1-5 mm, respectively ~~for the flight we analysed~~. However, saturation of DFR Ka/W for large aggregates can produce crossovers between DFR Ka/W and DFR X/Ka. ~~Reversely~~ Conversely, the strong connection between the particle size and the triple-frequency radar signature suggests that the data could be directly used ~~to produce look-up-tables for quantitative retrieval of particle size using measured mapping measurements in the (DFR Ka/W and, DFR X/Ka without prior knowledge of the overall cloud composition.)~~ space into microphysical properties like median volume diameter and effective bulk density with associated uncertainties. A first attempt is shown in Fig. ~~22a16a-b~~ where all data points from three ~~study~~ cases of the flight on ~~22 November 28~~ are used to ~~estimates~~ estimate MVD. In a similar way, effective bulk density of all data points can be averaged and mapped to the DFR plane (Fig. ~~22b16c-d~~). We find that, in general, effective bulk density of ice particles ~~decreases~~ increases as DFR X/Ka decreases and DFR Ka/W increases (ρ_e rotation feature) which is in a good agreement with findings in other airborne datasets (Chase et al., 2018, ~~Kneifel et al., 2015~~). These results look promising but the estimation errors could be high because different combinations of ice particles within the radar volume can produce similar triple-frequency signatures. Future improvement could be obtained by using more data points and a large set of scattering computations; a more quantitative analysis based on a Bayesian retrieval scheme is the topic of a companion study (Mroz et al., 2021b)).

625
630
635
640
645 With the high resolution grayscale imagery of ~~small~~ cloud ~~drops~~ particles from the CPI probe, we are able to identify signatures of different types of rimed particles. Regions with DFR Ka/W between [3-12] dB and DFR X/Ka between [2-68] dB are often connected to rimed particles with MVD < 6mm (although millimetre aggregates could also fit into this region). However, the shape of PSD also has noticeable ~~effete~~ effects on the distribution of DFR values (Mason et al., 2019). For the same characteristic size, data points with broader and flatter PSD ~~tend~~ tend to bend away from the horizontal curve (higher DFR X/Ka and lower DFR Ka/W). This feature was demonstrated in section D of segment 1 or in section B of the segment 2 where we observed rimed particles with MVD < 6 mm but DFR X/Ka > 8 dB and DFR Ka/W in the range of 6-8 dB. The distribution of rimed particles in the DFR plane found in this study spread in a much wider region than the findings ~~in of~~ Kneifel et al. (2015). On the other hand, large and low-density aggregates occurred in the region with both DFRs greater than 8 dB.

A multi-frequency system is ~~intended to be~~ useful because different frequencies are complementary (different sensitivities are exploited) and synergistic (non-Rayleigh scattering effects allow better microphysical retrievals, Battaglia et al., ~~2020b~~ 2020a). If the highest frequency radar is envisaged to provide sensitivity to small particles (e.g. like thoroughly demonstrated by

CloudSat) the lower frequencies must cover only the regions where non-Rayleigh effects become tangible. ~~Although the RadSnowExp data is very limited, it provides observational unique dataset radar sensitivity requirements for monitoring of arctic clouds.~~—A first clue about where this happens is provided in Fig. 2217. In a X-Ka band (and similarly a Ku-Ka band) system the lowest frequency ideally should reach at least down to 0 dBZ sensitivity to fully cover non-Rayleigh targets (right panel) with the
650 Ka-band system achieving sensitivities much better than that (thus far better than the current GPM-DPR); similarly in a Ka-W system the Ka-band sensitivity should go down to -5 dBZ (left panel). Recent developments in new technologies make these goals ~~at~~within reach (Battaglia et al, 2020b, Kummerow et al., 2020). Alternatively, an increased DFR dynamic range for small ice particles can be achieved by including observations at frequencies in the G-band (Battaglia et al, ~~2020b~~2020a, Lamer et al., 2021).

655 Closure studies that try to reconcile in situ PSD and IWC with remote sensing radar reflectivities remain challenging due to spatial variability of microphysics and mismatch between in-situ probe sampled volumes and radar backscattering volumes. Possible solutions can be provided by flight-direction forward or backward looking radars or adopting sophisticated phase coding schemes like Quadratic Phase Coding (Mead and Pazmany, 2019) to significantly reduce the blind zone close to the radar or multiple aircrafts coordinated flights.

660 *Acknowledgments.* This work is supported by the ESA RadSnowExp field project (Contract: 4000124359/18/NL/FF/gp), ESA RainCast project (Contract: 4000125959/18/NL/NA) and NRC. Many people from NRC, ECCC and Université du Québec à Montréal (UQAM) contributed for a successful completion of the campaign in a very challenging environment. We thank the engineering, operation and managerial staffs from NRC (E. Roux, J. Millett, S. Ingram, T. Van Westerop and D. Hoyi) and
665 ECCC (M. Harwood and J. Iwachow) who made the project possible by working long hours during instrument integration and field operations. The authors also would like to acknowledge the contributions of the ECCC science team (A. Korolev, D. Hudak, P. Rodriguez, and Z. Mariani) for their scientific advice and field support, J. P. ~~Blanche~~Blanchet and L. Pelletier of UQAM for forecasting support during the campaign.

References

- 670 [Abel, S. J., Cotton, R. J., Barrett, P. A., and Vance, A. K.: A comparison of ice water content measurement techniques on the FAAM BAe-146 aircraft, Atmos. Meas. Tech., 7, 3007–3022, <https://doi.org/10.5194/amt-7-3007-2014>, 2014.](#)
- Battaglia, A., Kollias, P., Dhillon, R., Roy, R., Tanelli, S., Lamer, K., Grecu, M., Lebsock, M., Watters, D., Mroz, K., Heymsfield, G., Li, L. and Furukawa, K.: Spaceborne Cloud and Precipitation Radars: Status, Challenges, and Ways Forward, Rev. Geophys., 58(3), doi:10.1029/2019rg000686, ~~2020b~~2020a.
- 675 Battaglia, A., Tanelli, S., Tridon, F., Kneifel, S., Leinonen J, Kollias, P.: Triple-frequency radar retrievals, chapter in the book Satellite precipitation measurement, Editor in Chief: Vincenzo Levizzani, Springer, ~~2020a~~2020b.
- Baumgardner, D., Abel S. J., Axisa D., Cotton R., Crosier J., Field P., Gurganus C., et al.: Cloud Ice Properties: In Situ Measurement Challenges, Meteorological Monographs 58, 9.1-9.23, 2017.
- [Bohren, C. F., & Huffman, D. R. \(1983\). Absorption and scattering of light by small particles. John Wiley & Sons, New York.](#)
- 680 Brown, P. R. A. and Francis, P. N.: Improved Measurements of the Ice Water Content in Cirrus Using a Total-Water Probe, J. Atmos. Oceanic Technol., 12, 410–414, [https://doi.org/10.1175/1520-0426\(1995\)012<0410:imotiw>2.0.co;2](https://doi.org/10.1175/1520-0426(1995)012<0410:imotiw>2.0.co;2), 1995.

Chase, R. J., Finlon, J. A., Borque, P., McFarquhar, G. M., Nesbitt, S. W., Tanelli, S., Sy, O. O., Durden, S. L. and Poellot, M. R.: Evaluation of Triple-Frequency Radar Retrieval of Snowfall Properties Using Coincident Airborne In Situ Observations During OLYMPEX, *Geophys. Res. Lett.*, 45(11), 5752–5760, doi:10.1029/2018gl077997, 2018.

685 [Decadal Survey \(Ed.\): Thriving on our changing planet: A decadal strategy for Earth observation from space \(p. 716\); Dias Neto, J., Kneifel, S., Ori, D., Trömel, S., Handwerker, J., Bohn, B., Hermes, N., Mühlbauer, K., Lenefer, M., and Simmer, C.: The TRIPLE-frequency and Polarimetric radar Experiment for improving process observations of winter precipitation, *Earth Syst. Sci. Data*, 11, 845–863, <https://doi.org/10.5194/essd-11-845-2019>, 2019.](#)
[Washington, DC: The National Academies Press, <https://doi.org/10.17226/24928>, 2017.](#)

690 Eriksson, P., Ekelund, R., Mendrok, J., Brath, M., Lemke, O. and Buehler, S. A.: A general database of hydrometeor single scattering properties at microwave and sub-millimetre wavelengths, *Earth Syst. Sci. Data*, 10(3), 1301–1326, doi:10.5194/essd-10-1301-2018, 2018.

[Faber, S., French, J. R., and Jackson, R.: Laboratory and in-flight evaluation of measurement uncertainties from a commercial Cloud Droplet Probe \(CDP\), *Atmos. Meas. Tech.*, 11, 3645–3659, <https://doi.org/10.5194/amt-11-3645-2018>, 2018.](#)

695 Gorgucci, E. and Baldini, L.: A self-consistent numerical method microphysical retrieval in rain using GPM dual-wavelength radar. *Journal of Atmospheric and Oceanic Technology*, 33, 2205–2223, 2016.

Haimov S., French J., Geerts B., Wang Z., Deng M., Rodi A., and Pazmany A.: Compact Airborne Ka-Band Radar: a New Addition to the University of Wyoming Aircraft for Atmospheric Research, IEEE International Geoscience and Remote Sensing Symposium, Valencia, Spain, 2018

700 Hamada, A. and Takayabu, Y. N.: Improvements in Detection of Light Precipitation with the Global Precipitation Measurement Dual-Frequency Precipitation Radar (GPM DPR), *Journal of Atmospheric and Oceanic Technology*, 33(4), 653–667, doi:10.1175/jtech-d-15-0097.1, 2016.

[Haynes, J. M., L'Ecuyer, T. S., Stephens, G. L., Miller, S. D., Mitrescu, C., Wood, N. B., and Tanelli, S.: Rainfall retrieval over the ocean with spaceborne W-band radar, *J. Geophys. Res.*, 114, <https://doi.org/10.1029/2008jd009973>, 2009.](#)

705 Heymsfield, A. J., Bansemer, A., Schmitt, C., Twohy, C. and Poellot, M. R.: Effective Ice Particle Densities Derived from Aircraft Data, *J. Atmos. Sci.*, 61(9), 982–1003, doi:10.1175/1520-0469(2004)061<0982:eipddf>2.0.co;2, 2004.

[Hiley, M. J., Kulie, M. S., and Bennartz, R.: Uncertainty Analysis for CloudSat Snowfall Retrievals, 50, 399–418, <https://doi.org/10.1175/2010jamc2505.1>, 2011.](#)

710 [Hogan, R. J. and Westbrook, C. D.: Equation for the Microwave Backscatter Cross Section of Aggregate Snowflakes Using the Self-Similar Rayleigh–Gans Approximation, *Journal of the Atmospheric Sciences*, 71, 3292–3301, <https://doi.org/10.1175/jas-d-13-0347.1>, 2014.](#)

Hogan, R. J., Tian, L., Brown, P. R. A., Westbrook, C. D., Heymsfield, A. J. and Eastment, J. D.: Radar Scattering from Ice Aggregates Using the Horizontally Aligned Oblate Spheroid Approximation, *Journal of Applied Meteorology and Climatology*, 51(3), 655–671, doi:10.1175/jamc-d-11-074.1, 2012.

715 [Hogan, R. J., Mittermaier, M. P., and Illingworth, A. J.: The Retrieval of Ice Water Content from Radar Reflectivity Factor and Temperature and Its Use in Evaluating a Mesoscale Model, *Journal of Applied Meteorology and Climatology*, 45, 301–317, <https://doi.org/10.1175/jam2340.1>, 2006.](#)

Hou, A. Y., Kakar R. K., Neeck S., Azarbarzin A. A., Kummerow C. D., Kojima M., Oki R., Nakamura K., and Iguchi T.: The global precipitation measurement mission, *Bull. Am. Meteorol. Soc.*, 95(5), 701–722, doi:10.1175/BAMS-D-13-00164.1, 2014.

720 Houze, R. A., Jr., McMurdie, L. A., Petersen, W. A., Schwaller, M. R., Baccus, W., Lundquist, J. D., Mass, C. F., Nijssen, B., Rutledge, S. A., Hudak, D. R., Tanelli, S., Mace, G. G., Poellot, M. R., Lettenmaier, D. P., Zagrodnik, J. P., Rowe, A. K.,

DeHart, J. C., Madaus, L. E., Barnes, H. C. and Chandrasekar, V.: The Olympic Mountains Experiment (OLYMPEX), *Bulletin of the American Meteorological Society*, 98(10), 2167–2188, doi:10.1175/bams-d-16-0182.1, 2017.

Iguchi, T., Kozu, T., Meneghini, R., Awaka, J. and Okamoto, K.: Rain-Profiling Algorithm for the TRMM Precipitation Radar, *J. Appl. Meteor.*, 39(12), 2038–2052, doi:10.1175/1520-0450(2001)040<2038:rpaft>2.0.co;2, 2000.

Kneifel, S., Leinonen, J., Tyynela, J., Ori, D., & Battaglia, A.: Satellite precipitation measurement. In (Vol. 1, chap. Scattering of Hydrometeors). Springer. (ISBN: 978-3-030-24567-2), 2020.

Kneifel, S., von Lerber, A., Tiira, J., Moisseev, D., Kollias, P. and Leinonen, J.: Observed relations between snowfall microphysics and triple-frequency radar measurements, *J. Geophys. Res. Atmos.*, 120(12), 6034–6055, doi:10.1002/2015jd023156, 2015.

Korolev, A., Emery, E., and Creelman, K.: Modification and Tests of Particle Probe Tips to Mitigate Effects of Ice Shattering, *30*, 690–708, <https://doi.org/10.1175/jtech-d-12-00142.1>, 2013a.

Korolev, A., Strapp, J. W., Isaac, G. A., and Emery, E.: Improved Airborne Hot-Wire Measurements of Ice Water Content in Clouds, *Journal of Atmospheric and Oceanic Technology*, 30, 2121–2131, <https://doi.org/10.1175/jtech-d-13-00007.1>, 2013b.

Korolev, A. V., Strapp, J. W., Isaac, G. A., and Nevzorov, A. N.: The Nevzorov airborne hot-wire LWC–TWC probe: Principle of operation and performance characteristics. *Journal of Atmospheric and Oceanic Technology*, 15(6), 1495–1510, 1998.

Kubota, T., Seto, S., Awaka, J., and Kida, S.: Evaluation of Precipitation Estimates by at-Launch Codes of GPM/DPR Algorithms Using Synthetic Data from TRMM/PR Observations, *IEEE J. Appl. Earth Obs. Remote Sens.*, 7, 3931–3944, 2014.

Kuo, K.-S., Olson, W. S., Johnson, B. T., Grecu, M., Tian, L., Clune, T. L., van Aartsen, B. H., Heymsfield, A. J., Liao, L. and Meneghini, R.: The Microwave Radiative Properties of Falling Snow Derived from Nonspherical Ice Particle Models. Part I: An Extensive Database of Simulated Pristine Crystals and Aggregate Particles, and Their Scattering Properties, *Journal of Applied Meteorology and Climatology*, 55(3), 691–708, doi:10.1175/jamc-d-15-0130.1, 2016.

Kummerow, C. D., Tanelli, S., Takahashi, N., Furukawa, K., Klein, M., and V. Levizzani, *Satellite precipitation measurement. In (Vol. 1, chap. Plans for Future Missions). Springer. (ISBN: 978-3-030-24567-2), 2020.*

Kulie, M. S., Hiley, M. J., Bennartz, R., Kneifel, S., and Tanelli, S.: Triple frequency radar reflectivity signatures of snow: Observations and comparisons to theoretical ice particle scattering models, *J. Appl. Meteorol. Clim.*, 53, 1080–1098, <https://doi.org/10.1175/JAMC-D-13-066.1>, 2014.

Lamer, K., Oue, M., Battaglia, A., Roy, R. J., Cooper, K. B., Dhillon, R., and Kollias, P.: Multifrequency radar observations of clouds and precipitation including the G-band, *Atmos. Meas. Tech.*, 14, 3615–3629, <https://doi.org/10.5194/amt-14-3615-2021>, 2021.

Lawson, R. P.: Effects of ice particles shattering on the 2D-S probe, *Atmos.-Le. M. and Chandrasekar, V.: Enhancement of dual-frequency classification module for GPM DPR, in: 2016 IEEE International Geoscience and Remote Sensing Symposium (IGARSS), IGARSS 2016 - 2016 IEEE International Geoscience and Remote Sensing Symposium, https://doi.org/10.1109/igarss.2016.7729550, 2016.*

Meas. Tech., 4(7), 1361–1381, doi:10.5194/amt-4-1361-2011, 2011.

Leinonen, J. and Szyrmer, W.: Radar signatures of snowflake riming: A modeling study, *Earth and Space Science*, 2(8), 346–358, doi:10.1002/2015ea000102, 2015.

Leinonen, J., Kneifel, S., Moisseev, D., Tyynela, J., Tanelli, S., and Nousiainen, T.: Evidence of nonspheroidal behavior in millimeter-wavelength radar observations of snowfall, *J. Geophys. Res.*, 117, n/a-n/a, <https://doi.org/10.1029/2012jd017680>, 2012.

[Lhermitte, R.: Attenuation and Scattering of Millimeter Wavelength Radiation by Clouds and Precipitation, *J. Atmos. Lerøy, D., Fontaine, E., Schwarzenboeck, A. and Oceanic Technol.*, 7, 464–479, \[https://doi.org/10.1175/1520-0426\\(1990\\)007<0464:aasomw>2.0.co;2\]\(https://doi.org/10.1175/1520-0426\(1990\)007<0464:aasomw>2.0.co;2\), 1990.](#)

[Strapp, J. W.: Ice Crystal Sizes in High Ice Water Content Clouds. Part I: On the Computation of Median Mass Diameter from In Situ Measurements, *Journal of Atmospheric and Oceanic Technology*, 33\(11\), 2461–2476, doi:10.1175/jtech-d-15-0151.1, 2016.](#)

765 Li, L., Heymsfield, G. M., Tian, L., and Racette, P. E.: Measurements of Ocean Surface Backscattering Using an Airborne 94-GHz Cloud Radar—Implication for Calibration of Airborne and Spaceborne W-Band Radars, 22, 1033–1045, <https://doi.org/10.1175/jtech1722.1>, 2005.

Li, H., Moisseev, D., and Von Lerber, A.: Dual-Polarization Radar Signatures of Rimed Snowflakes, in: 2018 IEEE International Conference on Computational Electromagnetics (ICCEM), 2018 IEEE International Conference on Computational Electromagnetics (ICCEM), <https://doi.org/10.1109/compem.2018.8496612>, 2018.

770 Lobl, E. S., Aonashi, K., Griffith, B., Kummerow, C., Liu, G., Murakami, M., and Wilheit, T.: Wakasa Bay, an AMSR precipitation validation campaign. *Bull. Am. Meteorol. Soc.*, 88, 551–558, 2007.

Mason, S. L., Hogan, R. J., Westbrook, C. D., Kneifel, S., Moisseev, D. and von Terzi, L.: The importance of particle size distribution and internal structure for triple-frequency radar retrievals of the morphology of snow, *Atmos. Meas. Tech.*, 12(9), 4993–5018, doi:10.5194/amt-12-4993-2019, 2019.

775 [Matrosov, S. Y.: A Dual-, Shupe, M. D., and Djalalova, I. V.: Snowfall Retrievals Using Millimeter-Wavelength Radar Method to Measure Snowfall Rate, *J. Appl. Meteor.*, 37\(11\), 1510–1521, *Cloud Radars*, 47, 769–777. \[https://doi.org/10.1175/1520-0450\\(1998\\)037<1510:adwrmt>2.0.co;2\]\(https://doi.org/10.1175/1520-0450\(1998\)037<1510:adwrmt>2.0.co;2\), 1998/2007/jamc1768.1, 2008.](#)

780 [Matrosov, S. Y.: Possibilities of cirrus particle sizing from dual-frequency radar measurements. *J. Geophys. Res.*, 98, 20675–20683, <https://doi.org/10.1029/93JD02335>, 1993.](#)

Mead, J. B. and Pazmany, A. L.: Quadratic Phase Coding for High Duty Cycle Radar Operation, *Journal of Atmospheric and Oceanic Technology*, 36(6), 957–969, doi:10.1175/jtech-d-18-0108.1, 2019.

Mróz, K., Battaglia, A., Kneifel, S., von Terzi, L., Karrer, M. and Ori, D.: Linking rain into ice microphysics across the melting layer in stratiform rain: a closure study, *Atmos. Meas. Tech.*, 14(1), 511–529, doi:10.5194/amt-14-511-2021, 2021a.

785 ~~Mróz~~ [Mróz](#), K., Battaglia, A., Nguyen, C., Heymsfield, A., Protat, A., and Wolde, M.: Triple-frequency radar retrieval of microphysical properties of snow, ~~submitted to~~ *Atmos. Meas. Tech.*, ~~2021~~ [2021](https://doi.org/10.5194/amt-14-7243-2021), 7243–7254, <https://doi.org/10.5194/amt-14-7243-2021>, 2021.

[National Academies of Sciences, Engineering, and Medicine, 2018, Thriving on Our Changing Planet: A Decadal Strategy for Earth Observation from Space, Washington, DC: The National Academies Press. <https://doi.org/10.17226/24938>.](#)

790 Nesbitt, S. W. and Anders, A. M.: Very high resolution precipitation climatologies from the Tropical Rainfall Measuring Mission precipitation radar, *Geophys. Res. Lett.*, 36(15), n/a–n/a, doi:10.1029/2009gl038026, 2009.

Nguyen, C., and Wolde, M., and Pazmany, A.: NRC W-band and X-band airborne radars: signal processing and data quality control, *Geoscientific Instrumentation, Methods and Data Systems Discussions*, in preparation, ~~2021~~ [2022](#).

795 [Nguyen, C., Wolde, M., Olson, W. S. et al.: GPM Combined Radar Radiometer Precipitation Algorithm Theoretical Basis Document \(Version 4\), 2016.](#)

[and Pazmany, A.: The NRC W- and X-band Airborne Radar Systems: Calibration and Signal Processing, 39th Conf. on Radar Meteorology, Iraka, Nara, Japan, *Amer. Meteor. Soc.*, 2019.](#)

Formatted: Font: 10 pt, Not Bold

- 800 Ori, D., Schemann, V., Karrer, M., Dias Neto, J., von Terzi, L., Seifert, A. and Kneifel, S.: Evaluation of ice particle growth in
 ICON using statistics of multi-frequency Doppler cloud radar observations, *Q.J.R. Meteorol. Soc.*, 146(733), 3830–3849,
 doi:10.1002/qj.3875, 2020.
- Petty, G. W. and Huang, W.: Microwave Backscatter and Extinction by Soft Ice Spheres and Complex Snow Aggregates, *Journal
 of the Atmospheric Sciences*, 67(3), 769–787, doi:10.1175/2009jas3146.1, 2010.
- 805 Praz, C., Ding S., McFarquhar G., and Berne A.: A Versatile Method for Ice Particle Habit Classification Using Airborne
 Imaging Probe Data, *Journal of Geophysical Research: Atmospheres* 123, no. 23, 2018.
- Protat, A., Delanoë, J., O'Connor, E. J. and L'Ecuyer, T. S.: The Evaluation of CloudSat and CALIPSO Ice Microphysical
 Products Using Ground Based Cloud Radar and Lidar Observations, *Journal of Atmospheric and Oceanic Technology*, 27(5),
 793–810, doi:10.1175/2009jtecha1397.1, 2010.
- 810 Stein, T. H. M., Westbrook, C. D. and Nicol, J. C.: Fractal geometry of aggregate snowflakes revealed by triple wavelength radar
 measurements, *Geophys. Res. Lett.*, 42(1), 176–183, doi:10.1002/2014gl062170, 2015.
- Stephens, G. L., Vane, D. G., Tanelli, S., Im, E., Durden, S., Rokey, M., Reinke, D., Partain, P., Mace, G. G., Austin, R.,
 L'Ecuyer, T., Haynes, J., Lebsock, M., Suzuki, K., Waliser, D., Wu, D., Kay, J., Gettelman, A., Wang, Z. and Marchand, R.:
 CloudSat mission: Performance and early science after the first year of operation, *J. Geophys. Res.*, 113,
 doi:10.1029/2008jd009982, 2008.
- 815 Schwarzenboeck, A., Mioche, G., Armetta, A., Herber, A., and Gayet, J.-F.: Response of the Nevzorov hot wire probe in clouds
 dominated by droplet conditions in the drizzle size range, *Atmos. Meas. Tech.*, 2, 779–788, [https://doi.org/10.5194/amt-2-779-
 2009](https://doi.org/10.5194/amt-2-779-2009), 2009.
- Tridon, F., Battaglia, A., Chase, R. J., Turk, F. J., Leinonen, J., Kneifel, S., Mroz, K., Finlon, J., Bansemer, A., Tanelli, S.,
 Heymsfield, A. J. and Nesbitt, S. W.: The Microphysics of Stratiform Precipitation During OLYMPEX: Compatibility Between
 820 Triple-Frequency Radar and Airborne In Situ Observations, *J. Geophys. Res. Atmos.*, 124(15), 8764–8792,
 doi:10.1029/2018jd029858, 2019.
- Tridon, F., Battaglia, A., and Kneifel, S.: Estimating total attenuation using Rayleigh targets at cloud top: applications in
 multilayer and mixed-phase clouds observed by ground-based multifrequency radars, *Atmos. Meas. Tech.*, 13, 5065–5085,
<https://doi.org/10.5194/amt-13-5065-2020>, 2020.
- 825 Tyynelä, J. and Chandrasekar, V.: Characterizing falling snow using multifrequency dual-polarization measurements, *J.
 Geophys. Res. Atmos.*, 119, 8268–8283, <https://doi.org/10.1002/2013jd021369>, 2014.
- von Lerber, A., Moisseev, D., Bliven, L. F., Petersen, W., Harri, A.-M. and Chandrasekar, V.: Microphysical Properties of Snow
 and Their Link to Ze-S Relations during BAECC 2014, *Journal of Applied Meteorology and Climatology*, 56(6), 1561–1582,
 doi:10.1175/jamc-d-16-0379.1, 2017.
- 830 Westbrook, C., Aichert, P., Crosier, J., Walden, C., O'Shea, S., Dorsey, J., and Cotton, R. J., 2018: Scattering Properties of
 Snowflakes, Constrained Using Colocated Triple-Wavelength Radar and Aircraft Measurements, 15th Conference on
 Atmospheric Radiation, Vancouver, BC, Canada, Amer. Meteor. Soc., 9-13 July, 2018.
- Wolde, M. and Co-authors: Radar Snow Experiment ~~For Future Precipitation Mission~~ for future precipitation mission
 (RadSnowExp), Living Planet Symposium, Milan, Italia, 13-17 May 2019.
- 835 ~~Wolde, M., and Pazmany A.: NRC dual-frequency airborne radar for atmospheric research. 32nd Conf. on Radar Meteorology,
 Albuquerque, NM, Amer. Meteor. Soc., P1R.9,-2005.~~
- ~~Wolde, M., Battaglia, A., Nguyen, C., Pazmany, A. L., and Illingworth, A.: Implementation of polarization diversity pulse pair
 technique using airborne W band radar, *Atmos. Meas. Tech.*, 12, 253–269, <https://doi.org/10.5194/amt-12-253-2019>, 2019.~~